C. ELEGANS AND MICROBEAM MODELS IN BYSTANDER EFFECT RESEARCH

A Dissertation

by

SHAOYONG FENG

Submitted to the Office of Graduate and Professional Studies of
Texas A&M University
in partial fulfillment of the requirements for the degree of

DOCTOR OF PHILOSOPHY

Chair of Committee,	Leslie A. Braby
Committee Members,	John Ford
	Warren D.Reece
	Keith Maggert
Head of Department,	Yassin A. Hassan

August 2013

Major Subject: Nuclear Engineering

ABSTRACT

Radiation induced bystander effects have changed our understanding of the biological effects of ionizing radiations. The original assumption was that biological effects require direct damage to DNA. The bystander effect eliminated that requirement and has become one main stream in radiation research ever since first reported over 20 years ago.

Most bystander studies to date have been carried out by using conventional single cell *in vitro* systems , 2D cell array and 3D tissue samples, which are useful tools to characterize basic cellular and molecular responses. But to reveal the complexity of radiation responses and cellular communication, live animal models have many advantages. In recent years, models such as *C. elegans* and Zebrafish have been utilized in bystander effects research. In the Loma Linda/TAMU experiment, a L1 larva *C. elegans* model was devloped to study the radiation bystander effects by irradiating single intestine cell nuclei with a microbeam of protons.

Due to the stochastic nature of particle interactions with matter and changing stopping power when protons slow down, precise dosimetry in the target nucleus is a difficult problem. This research was undertaken to provide a detailed description of the energy deposition in the targeted and surrounding non-targeted cell nuclei, and to evaluate the probabilities of the non-targeted cell nucleus being irradiated. A low probability is required to exclude the possibility of radiation biological effects in non-targeted cells is caused by scattered particles.

Mathematical models of the microbeam system and the worm body were constructed in this research. Performing Monte Carlo simulations with computer code,

Geant 4, this research provided dosimetry data in cell nuclei in different positions and probabilities of scattering to non-targeted cell nuclei in various microbeam collimator configurations. The data provided will be useful for future collimated microbeam design.

DEDICATION

This dissertation is dedicated to my fiance and immediate family members: my mom, dad and sisters. Thank you for all of your love, support, and sacrifice through my life.

ACKNOWLEDGEMENTS

First and foremost, I would like to thank my advisor Dr. Leslie A. Braby for his direction and discussion. Without him I would not have achieved my goals for this dissertation.

I would like to thank Dr. Warren D. Reece for the financial support for my graduate study.

I would like to thank my advisory committee for their guidance and the knowledge they've passed on to me.

I would like to thank my family members. Their unconditional support and encourage have helped me overcome all of difficulties.

Finally, I would like to thank my fiance. Without her love, support, and sacrifice I never would have realize my full potential.

NOMENCLATURE

CSDA	Continuous Slowing Down Approximation
LET	Linear Energy Transfer
LNT	Linear No-Threshold
RBE	Radiation Biological Effectiveness
TAMU	Texas A&M University

TABLE OF CONTENTS

LIST OF FIGURES

FIGURE Page

LIST OF TABLES

TABLE Page

1. INTRODUCTION AND BACKGROUND

Since the discovery of ionizing radiation, it has been known that ionizing radiation can damage living cells and tissues, and research on biological effectiveness of radiation has been a focus area in radiation studies.

Lots of research has been done on the relationship between radiation risks and radiation absorbed dose, quality factors and radiation sources. High dose exposures are considered to be harmful to human body without doubt. Based on intensive studies of the Japanese atomic bomb survivors and survivors of several nuclear accidents in the world, a lot of data about the carcinogenic risks and non-cancer risks have been reported. Many experiments, both *in vitro* and *in vivo*, were performed to study the biological effects of radiation at a relatively high dose level. For low dose irradiation, in spite of intense studies on the radiation effects, there remain a lot of uncertainties in the relationship between the dose and radiation risks. In radiation protection, excess cancer risk associated with low dose radiation exposure is usually estimated by the Linear Non Threshold (LNT) model for precaution, which means extrapolating the low dose risks on the basis of what is observed in the population exposed to high doses and on the basis of experimental data obtained at high dose.

It has always been the dogma of radiation biology that the deleterious effects of ionizing radiation are due mainly to direct damage to DNA from the action of irradiation or from very short lived free radicals generated by it. Furthermore, for over a century since the discovery of X-rays, the course of biological consequences was assumed to be limited to the target cells or their progeny for one or two cell generations. The report of bystander effects revealed that direct radiation exposure is not required for cells to express radiation induced damage. The experimental

evidence of the bystander effect might result in a change in the dose response curve in the low dose region.

1.1 Bystander effects

The term, radiation-induced bystander effect, is used to describe radiation-induced biological effects in cells that are not directly traversed by a charged particle. Bystander cells can be adjacent, within a few cell diameters, in a different organ, or even in a different animal to the irradiated cells. In most systems the bystander cells are unirradiated, although in some cases the bystander signalers and responders both receive some radiation dose [1].

Bystander effects was first reported by Nagasawa and Little [2] who observed that, following a low dose of alpha particle irradiation, increased frequency of sister chromatid exchanges was observed in 30% of cells even though less than 1% of cell nuclei were transversed by an alpha particle. Bystander effects have been intensely studied, in the last 20+ years after bystander effects became part of the radiobiology vocabulary, using a wide variety of radiation sources, which differed in their radiation quality. In addition to the most commonly examined radiation sources, such as alpha, beta, x rays and gamma rays, bystander effects have been investigated after irradiations with protons, high-energy electrons, Auger electrons, and heavy particles [1]. Linear energy transfer (LET) dependence has been observed in several studies by comparing bystander effects induced by different radiations [3, 4] or induced by the same radiation but at different energies [5]. Bystander effects have been demonstrated for both high- and low-LET radiations but the effect is usually much more pronounced for densely ionizing radiation [6]. Radiation source dependences have also been observed in several studies. In some cases, bystander effects can be observed after exposure to one radiation source but not another [1].

As with the radiation source and LET, absorbed dose has also been shown to be related with bystander effects in various studies. However there is no simple relationship between the magnitude of effects induced and the absorbed dose. Irons, *et al.* [7] reported that the relationship between bystander effects and dose is different depending on the biological process. In *in vitro* cultures of cells, transforming growth factor-beta (TGF-beta) levels increased with the dose, however the levels of tumor necrosis factor-alpha (TNF-alpha) were increased only for higher x-ray doses. For alpha particles, several studies have revealed that some biological effects such as survival and the frequency of oncogenic transformation in bystander cells depend on the dose to the irradiated cells. But other studies, usually in different cell lines, indicated that the magnitude of the bystander effect induced is similar when comparing single and multiple alpha particles traversals to one or more cells (see [1]). A dose threshold is also observed by Liu *et al.* [8] who found that there were no radiation effects induced in unirradiated cells for x- or gamma-ray doses below several mGy to the irradiated cells. A lack of a bystander response with neutrons occurred up to about 1 Gy.

For purposes of radiation protection the LNT model has been used to extrapolate the risks of health effects of ionizing radiation exposure at low doses from known high dose date since the 1970s. Bystander studies showed that in a narrow range of low doses the radiation risks are much larger than the results extrapolated by the LNT model [9]. Due to bystander effects, the target for the biological effects of radiation is larger than the cells irradiated, so the responses of tissues to low-dose radiation cannot be reduced to a summation of individual cell responses. Besides the low dose region, the shape of the dose-response curve for radiation-induced carcinogenic risk in the dose region that is relevant for the majority of the population may also be influenced by bystander effects [6, 1, 10].

Bystander effects have received considerable attention and have remained a focus of low-dose radiobiology research since they were reported. The relationship with absorbed dose, LET, type of radiation, and signal communication between targeted and non-targeted cells have been intensely studied. But there is still lots of uncertainty in the bystander effects area, such as the radiation risks to human body for low dose radiation, despite significant progress and numerous data published.

The initial bystander experiments were conducted using low dose broadbeam radiation, and conclude the induction of effects in unirradiated cells by relying on statistical methods [2, 3]. The number of cell nuclei to be directly irradiated was calculated by the total number of primary particles emitted from the radiation source and the ratio of the cross-sectional area of the cell nucleus to the whole area of the 2D cell array, assuming that one radiation particle could only transverse one cell in the 2D cell array. When discussing the impact of bystander effect in the context of carcinogenic risk at low radiation doses delivered by a uniform radiation source, the relevant dose range *in vivo* is limited to traversal by a few ionizing tracks per cell at most, since exposures that result in higher numbers of traversals will not leave unirradiated cells within the irradiated volume (Figure 1.1). About 60% of cells do not receive any hits if the hits per cell is only 0.5, and the fraction of cells that do not have any radiation transverse decreased quickly as the dose increase. If only 1% of cells are desired to be directly irradiated, the mean number of hits per cell should be restricted to 0.01. The doses are limited to very low level, depending on the LET of the source radiation and cell dimensions. In addition, in the radiobiology experiments using broad beam irradiation, usually it is hard to satisfy the need to observe effects in both directly irradiated and unirradiated bystander cells, as it is impossible to distinguish directly irradiated and unirradiated bystander cells. With a microbeam, however, the irradiated cells can be identified using their positions.

The bystander problem has inspired a variety of novel experimental methods such as the charged-particle microbeam and x-ray microprobes [1].

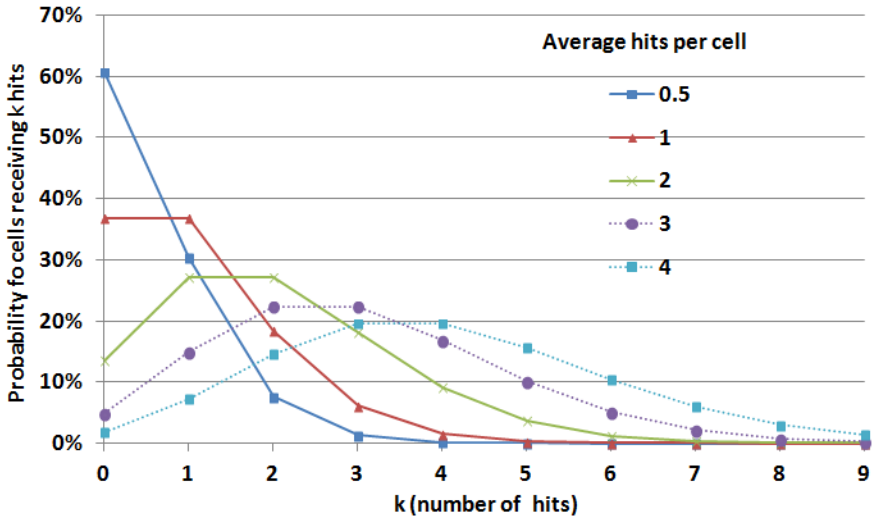

Figure 1.1: Probablity distributions of number of hits per cell when the mean number is 0.5 through 4. Only 15% of cells receive 0 hit, when the mean is 3. And the proportion declines for larger mean values

The use of microirradiation techniques in radiation biology dates back to the 1950s to the work of Zirkle and colleagues [11]. They designed methods to generate microbeams of protons and alpha particles to irradiate a small fraction of average-sized cells. While these earlier studies with microbeams were highly innovative, they did not eliminate the random variation around the specified average dose. Recent developments in microbeam technology have made drastic improvements in particle delivery, focusing, target imaging and precision to allow for rapid advances in our knowledge in radiation biology.

The development of single particle microbeams, where a single cell and/or a

subcellular compartment can be selectively irradiated with one or multiple particles, has greatly facilitated our understanding of a variety of biological endpoints including cytoplasmic irradiation, bystander effects and genomic instability. With advances in microbeam technology, it has been possible to demonstrate unequivocally that cells and tissues that are not directly exposed to radiation, but merely in the vicinity of ones that are, can contribute to the radiobiological response; this represents a major paradigm shift in our understanding of the target theory and other low dose phenomena. There is increasing evidence that the non-targeted response can equally be demonstrated in multicellular organisms using a microbeam [12].

Various cell-lines have been used in the microbeam based bystander effects studies, revealing bystander effects in different biological target end points. Such bystander effects research has often been undertaken using microbeam irradiation of individual cells plated in 2-D monolayer and recently in 3-D tissue like constructs, to study the intercellular communications in order to reveal the mechanisms of bystander effects. Use of whole organisms for microbeam studies has many advantages over the 2-D and 3-D tissue like cell matricies, because the whole organisms have a multicellular morphology and communications between cells. Several organisms have been used in the microbeam bystander effects studies, such as *Arabidopsis thaliana*, *Bombyx mori* and *C. elegans*. In the Loma Linda/TAMU experiments L1 larva *C. elegans* were used to study the bystander effects in the intestine cells. The simple culture conditions and maintenance, rapid life cycle, short life span, fully sequenced genome, transparent body, and small number of somatic cells make *C. elegans* a suitable model for in *in vivo* microbeam studies to investigate bystander effects in whole organisms.

1.2 *Caenorhabditis elegans*

Caenorhabditis elegans (*C. elegans*)is a small nematode, commenly found in garden soil, feeding on soil bacteria. With a simple and straight biological structure, *C. elegans* adult has only 900-1100 cells in total. Similar to other nematodes, the life cycle of *C.elegans* is comprised of the several different stages: embryonic stage, four larval stages(L1-L4), and adulthood.

During embryonic development, cell division progresses from a single cell to about 550 essentially undifferentiated cells and as it progresses through the larval stages it takes form as an animal with fully differentiated tissues and organs. At the end of the embryo stage, there are four germ cell precursors, Z1 to Z4. The main body plan of the animal is already established at the end of embryogenesis. During L1 to L4 stage, the nervous system and reproductive system develops. The general body plan does not change during post-embryonic development.

In the Loma Linda/TAMU experiment, the L1 larval are irradiated and specific intestine cells are targeted. The microbeam protons or alpha particles are aligned with the target nucleus. The intestine is comprised of 20 large epithelial cells that are mostly positioned as bilaterally symmetric pairs to form a long tube around a lumen. The ancestor of these cells is the E blastomere cell, which is born on the surface of the embryo about 30 minutes after fertilization. The intestinal development is divided into specific stages which are indicated by the number of E descendants present, such as E2, E4, E8, E16, and E20, although occasionally due to an extra cell division during development the mature intestine is seen to be made of 21 cells instead of the usual 20. Each of these cell pairs forms an intestinal cell ring. The anterior most is an exception and is comprised of four cells. The intestine has distinct apical, lateral, and basal regions. Each intestinal cell forms part of the intestinal lumen at its apical

pole and secretes the constituents of the basal lamina from its basal pole. Each intestinal cell is sealed laterally to its neighbors by large adhered junctions close to the apical side. It also connects to the neighboring intestinal cells via gap junctions on the lateral sides. During development, int II, int III and int IV rings initiate a coordinated 90 degree rotation, however, it seems to be variable. The orientation of cells in the adult int VI-IX rings is variable too. Rings VI-VIII tend to adopt left-right positions, whereas ring IX cells are usually positioned dorsoventrally. As the animal ages, the intestine does not fill the entire cavity behind the pharynx, instead, it becomes deflected to permit the growth of the gonad within the same cavity.

The outer surface of *C. elegans* is covered by a tough, but flexible, extracellular cuticle, which protects the animal from the environment, maintains body shape, and permits motility by acting as external support. Initially the adult cuticle is approximately 0.5 um in thickness, with aging, the thickness of the adult cuticle increases. Larval stage cuticles differ from adult in the type of layers present or their relative thickness. Under the hypodermis, there is a layer of muscle cells, which are arranged in four longitudinal bundles located in four quadrants.

In bystander effects research using microbeams, clearly demonstrating the probability of non-targeted cells to be irradiated is necessary and required to exclude the possibility that the bystander effects are induced by direct transverse by scattered particles. In addition the energy deposition in the target cells, which is difficult to measure, is helpful to evaluate the bystander effects, especially when studying the relationship of bystander effects and absorbed doses. With the known structure of intestine zone in the worm body, dosimetry in a particular cell nucleus, which is difficult to achieve in experiments, is possible with a detailed computer model. And the scattering to other cell nuclei can be investigated in different microbeam configuration.

2. EXPERIMENTAL SETUP

As discussed above, bystander effect studies has inspired the development of microbeam equipment, which can deliver precise numbers of particles to part of the target cell. With microbeam irradiation targeting on one or several identifiable cells, distinguishing the directly irradiated cells and unirradiated bystander cells is possible. High spatial resolution is crucial in studies regarding cell-to-cell communications, functionality of sub-components within the cell, and intercellular communications. Depending on the questions to be addressed, the requirement of beam diameter ranges from several micrometers down to nanometer level. Several micrometer resolution is most common and sufficiant to limit the irradiation to one particular cell without irradiating the surroundings. Better spatial resolutions are required, however, to precisely irradiate subcellular components. In future developments, sub-micrometric beams may be required to target a single gene. In the Loma Linda/TAMU experiment, a 5 micrometer diameter particle beam is constructed to meet the requirement of the bystander effect research in *C. elegans*.

2.1 Methods of generating microbeams

In order to limit the irradiation to a specific cell in a population or to a specific site in a cell, the accelerated beam of charged particles has to be reduced to a micrometric or sub-micrometric size. There are two methods to accomplish this requirement: collimation or focusing, magnetically or electrostatically.

Collimation, which is first introduced by Zirkle [11] is an easier way to narrow radiation beams, reducing the fluence to a relevant level for low dose irradiation. The main limitation of mechanical collimation is the scattering of particles on the inside walls of the apertures, which increases in proportion to the ratio of the perimeter to

the area of the aperture [13]. Scattering will produce particles with lower energies and wider lateral angles than the primary beam. Collimator material and the geometry have to be properly optimized to minimize the scattered component and improve the beam quality. Coupled collimators are often applied to reduce the scattering, with the first one narrowing the beam and the second stopping the particles scattered by the first. Also, alignment of the collimators with respect to the incoming beam is a very delicate task. Several solutions for collimation and collimator alignment systems have been adopted at different laboratories developing microbeam by mechanical methods.

Focusing has higher spatial resolution, and can be used to target smaller cellular structures than mechanical collimation. The narrowest beam the focusing method can achieve is down to sub-micrometeric size, so it has a high spatial resolution and targeting accuracy in vacuum. However, the vacuum window which is required to introduce the beam from vaccuum to the target, would reduce the performances due to scattering. And the cost of installing a focused system is usually greater than setting up a collimated microbeam. Focused beams are used widely in non-radiobiological applications which can benefit from their high beam current and precision, but they are problematic for low dose radiations. The intense beam generated by the focusing system makes it difficult to deliver precise numbers of particles to the target cell, which usually requires only several particles.

2.2 Collimator setup

In the Loma Linda/TAMU experiment, a collimated microbeam system was built to narrow the wide charged particle beam generated by the accelartor to the required diameter. As shown in the Figure 2.1, the collimator system includes the lower adjustable steel aperture, control shutter, copper aperture and Mylar sample holder.

The charged particle beam, which has a large diameter and is essentially monogenetic is generated by an electrostatic accelerator. The radiation beam was initially narrowed down to about 3-micrometer square by the adjustable aperture, which consists of 4 steel blades. In the experiment, the steel blades were carefully adjusted to narrow down the radiation beam to about 3 μm X 3 μm, and at the same time making sure it is aligned with copper aperture. The alignment is achieved by positioning each steel blade to reduce the beam fluence through the copper collimator without stopping it. Some particles in the result are scattered by interactions with the edge of the steel blade. The scattered particles are blocked by the copper collimator, which is 25 μm in thickness with a 5 μm diameter laser drilled hole in the center. Because the copper collimator is about 30 cm away from the steel aperture, most scattered primary particles and delta rays cannot travel through the small collimator hole. The larger size of the copper hole than the steel aperture window avoids interactions of source beam and the copper edge. The hadron particles are introduced to the air from the vacuum after passing through thin Mylar®which includes the sample holder and a window to seal the collimator hole. The target nucleus in the worm can be aligned with the radiation beam as it is close to the copper hole.

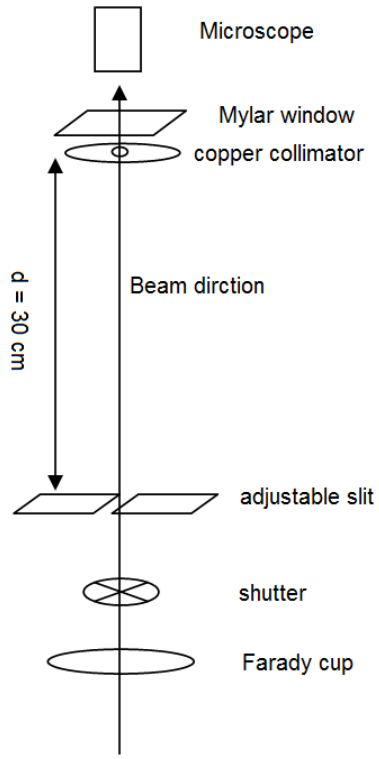

Figure 2.1: The schematic of the collimator setup in Loma Linda/TAMU bystander effect experiments

In the Loma Linda/TAMU experiments, each targeted cell was irradiated by about 25 protons by controlling the shutter to give the same product of fluence rate and shutter open time. As the average fluence is fixed, the total number of particles that reach the target would be random and following Poisson distribution. For experiments requiring lower fluence, a thin scintillator can be mounted between the copper collimator and the sample holder to measure the number of primary particles that can reach the target[14]. In those experiments, the signal from the scintillator is used to control the operation of the shutter, so the exact number of primary particles can be delivered to the target cell.

3. MODELS AND SIMULATION

The collimator-based microbeam facilities are easier to construct compared with a focusing system, but collimated systems also have some limitations including low intensity, scattering from the collimator edges, the need to place the target close to the collimator [15], and the need for precise alignment of collimator components.

Energy deposition in the target cell or nucleus is the quantity needed by the radiation biologist, especially when the relationship between the absorbed dose and bystander effects is the research interest. In the microbeam irradiation system, low energy particles are usually used and the target is usually located near the end of the charged particle track. The absorded dose to the target can be estimated by continuous slowing down approximation (CSDA), but Bragg Peak effects and particle energy straggling, after traveling through sample holder, scintillator detector, and the tissue before reaching the targeted area, would increase the uncertainty of the dose in the targeting area. The probabilities of non-targeted cells or cell nuclei being irradiated by scattered particles are also important in bystander effect studies. The probabilities should be very low in order to exclude the possibility that biological effects in non-targeted cells or cell nuclei are caused by scattering rather than by bystander signals.

In order to evaluate the scattering and energy deposition in specific targets for different microbeam system configuration, a mathematical model of the microbeam facilities and the target organisms was developed. The model was built using Geant4, which is a popular Monte Carlo simulation package and is widely used in radiation track structure simulations. The geometry setup mainly includes two parts, the collimator system and the worm body. The collimator system model was constructed

according to the experimental setup shown in Figure 3.1. The model of the *C. elegans* body was built according to the cell position in the body as shown in the Figure 1.2, and the distance between any two nuclei and their angles relative to the vertical section are selected according to the data in [16, 17], although the number may vary slightly in individual worms.

3.1 Collimator models

The Figure 3.1 shows the plot of Geant4 model of the microbeam system, including an adjustable steel aperture, a copper aperture and a sample holder. In the simulation, a wide beam of monoenergetic charged particles was used to simulate the original radiation beam source generated by the accelerator. The directions of charged particles from the accelerator are essentially identical and the standard deviation of the energy is small compared to the total energy, so the ideal wide radiation beam can be used to represent the radiation source without modeling the complex accelerator. The shutter in the experimental setup (Figure 2.1) is used to control the irradiation time interval in order to control the total number of particles delivering to the target. During a shutter open period, although only a small number of particles can reach the target, a large number of source particles was generated by accelerator. In the simulation, the shutter was not built and a fixed total number of source particles is used to simulate the shutter open time. Because the relative variation of the a large number of particles is very small, a fixed number of source particles can closely simulate the shutter open time.

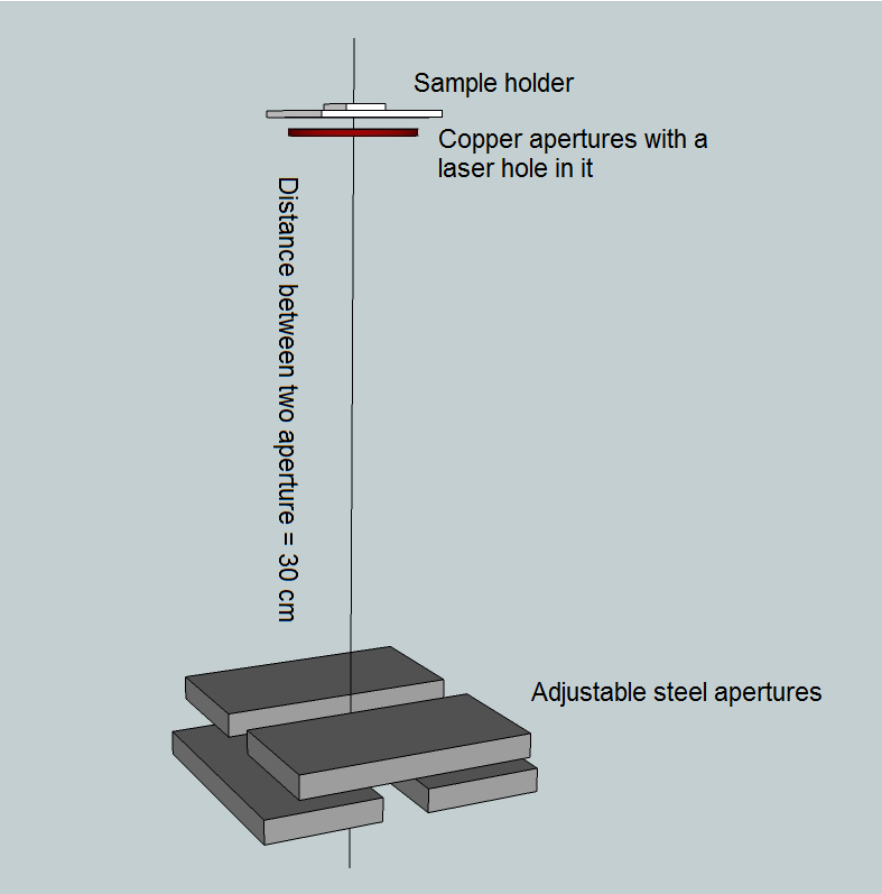

Figure 3.1: The computer model built to simulate collimated microbeam. The lower aperture was formed by four adjustable steel blades, and the upper one is a copper sheet with a laser drilled hole in it. The scale for different parts may vary

The aperture models and their shapes significantly affect the radiation scattering, so it is very important that the shape is accurately modeled. For an ideal shape steel aperture and copper aperture, the scattering is negligible. Because the source particles travel parallel to the surface of the rectangular steel blade and the inner wall of the copper hole, the only scattering is from the interactions of charged particles hitting the edge of the steel aperture. In experimental conditions, there is always an angle between the radiation direction and the aperture wall.

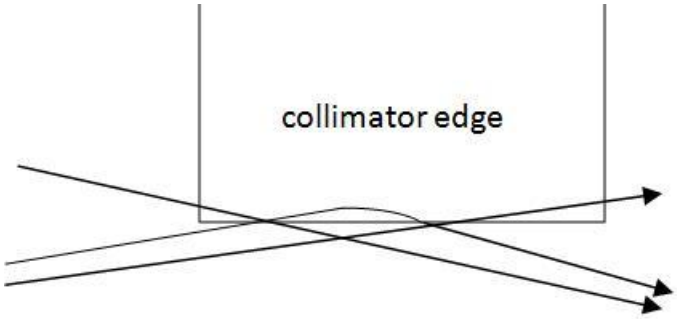

Figure 3.2: Scattering from the surface of the collimator

Figure 3.2 shows the different types of scattering at blade edges when the radiation beam is not parallel to the aperture wall. The scattering will increase the number of lower energy particles with changed directions. With an rough surface, the scattering would be increased substantially. In the simulation, several different steel aperture surface models were built to study the scattering effects to the results.

The model of the copper aperture has a significant effect on the results because the distance from it to the target is only several micrometers, and any scattering from the copper could contribute to the dose to the target. Laser drilled small diameter holes are used in several microbeam facilities ([18]), the small laser drilled holes in metal provide an easy way to generate microbeams, but they have several disadvantages making them less than ideal for the collimation microbeam system. Laser drilled holes usually have poor surface finish, because the metal melting pattern is not symmetric and some ablated material is redeposited on the inside of the holes [19]. The hole produced by laser drilling is tapered, with a larger entrance and smaller exit (laser beam entrance/exit when drilling), which will increase the scattering and degrade the energy spectrum. Due to the asymmetry and rough inner wall surface, a large diameter should be selected to make sure the smallest diameter of the hole

is larger than the diameter of the first aperture.

In the simulation, very detailed models of copper aperture were built to simulate the inner wall surface with different exit and entrance diameter ratios.

3.2 Worm body models

A detailed model of the worm was built to estimate the dose delivered to the targeted cell nuclei. Figures 3.3 shows the transverse section of intestine model for the L1 worm. The dimensions of skin, muscle, and hypodermal tissue were set according to the transverse section images in the refrence[16]. In the model, different atomic compositions were built for different tissues, although in this study the atomic composition has negligible effects on the dose distribution or scattered particles. For low energy x-rays, the atomic composition could have a significant effect on dose deposition in target area. The worm model developed for this study is expected to be useful for other bystander effect research using x-ray beams.

In the model, all 20 intestine cells in L1 stage worm were built, cell dimensions and nucleus positions were set according to measured data[17]. The location of intestine cell nuclei in worm body varies in different worms, but the standard deviation of the locations is small for L1 stage worm[20]. Due to the low variation, the model using average cell nucleus locations could represent realistic worms. Measured data shows the average diameter of intestine cell nuclei is 3.23 μm [20], and the dose deposition date shown in this work were based on the average diameter. For larger or smaller cell nucleus the absorbed dose will be slightly different.

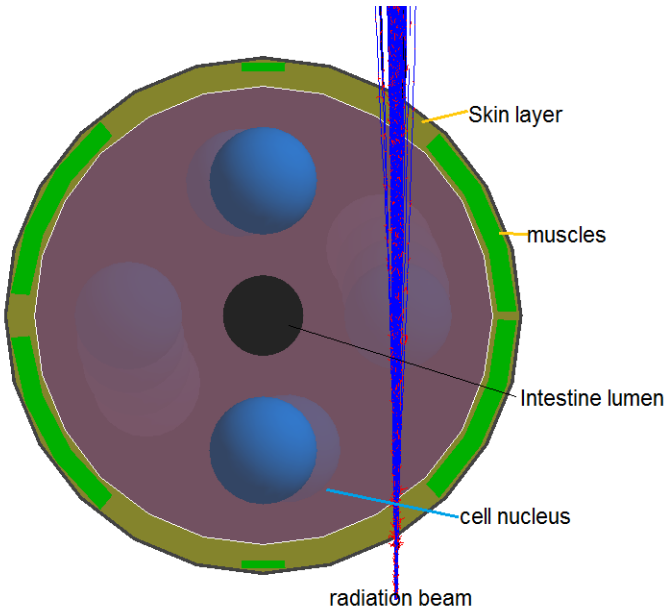

Figure 3.3: A transverse view of the worm computer models

3.3 Scintillator and sample holder models

For low fluence studies a scintillator detector is required between the collimator and the target, providing signals to control the shutter, in order to facilitate experiments when exact number of particles is required. The thin layer of scintillator, which is about 10 micrometers thick, absorbs a fraction of the particle's energy, widens the energy spectrum and weakens the targeting accuracy. Scattered particles from the aperture edges could be stopped in the scintillator, as a results the number of particles delivered to the target is different from the output of the detector. In the simulation, the effects of scintillator and Mylar®sample holder on scattering were also studied to provide references for the experiments.

4. RESULTS AND DISCUSSION

In order to calculate the limitations of the collimated microbeam, simulations using the computer model focused on the beam scattering and energy deposition. The purpose was to clearly demonstrate the probability of non-targeted cells being irradiated by scattered particles and to provide biologists the dose distribution in the target cell nuclei for different collimator setups. The Geant 4 code was used to simulate single particle interactions in the collimator system and the worm phantom. So the probability that a single proton will irradiated a non-targeted cell nucleus and the energy deposition spectrum in target could be estimated by simulating a large number of particles.

In this chapter, the best microbeam quality that can be generated in the collimator system of the Loma Linda/TAMU experiments was evaluated, by simulating an ideal condition collimator. Any requirement beyond the results should be pursued by alternate methods, like focusing. Simulations of scattering on different part of collimators and the smallest diameter of the beam the collimation system can generated were performed and the results were analyzed in this part. The results will aid future collimator design efforts by providing information to select the best collimator diameters and other physical properties, and providing information on what should be addressed to improve the system performance.

The energy deposition in a targeted cell nucleus is randomly distributed because the particle track length in the spherical nucleus depends on the position where the charged particle enters, and the random process of the interaction of charged particles with materials. The simulation result for the energy delivered to the target by a single particle is meaningless, instead we provided energy deposition distributions in the a

target cell nucleus by simulating large number of particles.

4.1 Beam scattering

The effect of the scattering from the collimators on the microbeam is the primary issue for the simulation. Scattering is one of the several limitations on microbeam precision and is controled by mechanical collimators. Due to scattering, the diameter of the beam, when it reaches the target, is larger than its original size when it is traversing the final collimator aperture. Folkard *et al.* [21] measured values of the scattering from a 1 μm diameter aperture. They found that 4% of the protons were at least 5 μm away from the mean position and 10% were at least 2 μm away. Gerhard *et al.* [18] published that 92% of the particles were within the nonscattered core of the 5 μm collimator beam produced by their dual aperture collimator. Besides effecting the diameter of the beam, energy loss is another result of the particles hitting the collimators. In the Folkard *et al.* [21] experiment, the mono-energetic proton beam was spread out into a spectrum with a full-width at half-maximum energy of 47keV for the main peak, and about 96% particles fell within this full energy peak. Scattering is related to the shape of the collimators and the geometry of the system. Theoretically, the scattering is proportional to 1/r, in which r is the diameter of the collimator. Also the thickness of the aperture has a large effect on the scattering. The system should be clean, straight and properly aligned to reduce the scattering effects. In the following sections, the effects of scattering on the dual collimators, and alignment effects are discussed.

4.1.1 Ideal shape colliamtors

To investigate the characteristics of the best microbeam a collimation system can generate and reveal the theory of the collimated microbem, an ideal collimator model was built . In ideal conditions, the steel aperture blades were built in a rectangular

shape with smooth surface which is parallel to the direction of source particle beam. The copper aperture has a tubular hole without laser drilling debris on the inner wall, and the diameter is a little larger than that of the first aperture. The two apertures are perfectly aligned.

Due to the larger diameter of the second aperture, the main beam particles which travel through the first aperture will cleanly pass the second aperture without any interactions. Any scattered and partial energy particles that could reach the target tissue would be sacttered from the edge of the steel blades. Figure 4.1 shows scattering of particles interaction with the steel aperture blade, when there are 200 particles in the main beam. To illustrate the scattering interaction between the particles and steel blade, particles which cleanly pass the aperture is not plotted. About 20 primary particles were scattered back to the main beam, but they quickly reached another point on the aperture blade and were stopped. With thick aperture blade, the probabilities of scattered particles travel through the collimator aperture are lower. So in some microbeam sytems where only one collimator is used to narrow the source radiation beam, a thick collimator was usually preferred to reduce scattering.

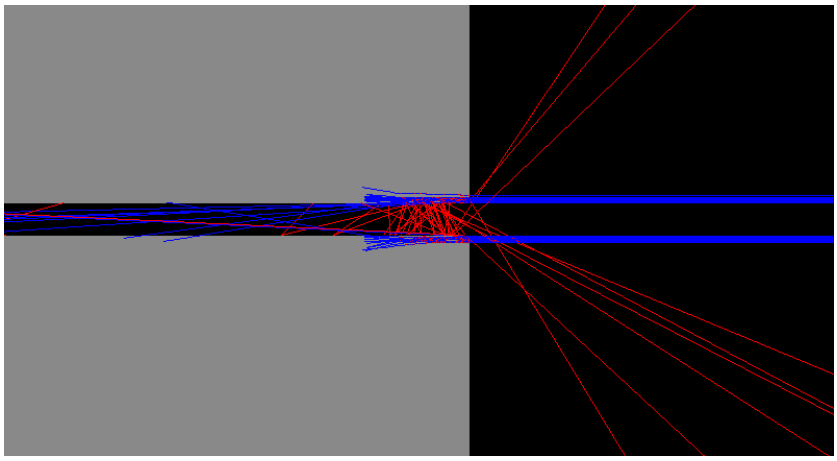

Figure 4.1: Charged particle scattering near the edge of the steel aperture in the ideal conditions. To clearly demonstrate scattering, the primary particles which passed through the aperture without interactions were not plotted. Distance between the two aperture blade is 3 μm. Blue line: protons; Red line: delta rays; Grey: steel blades

In order for the scattered particle to arrive at the target tissue, the scattering angle which is between the direction of scattered particles and the blade surface must be very low, because of the large distance between the two apertures. In the Loma Linda/TAMU bystander effects experiments, the maximum angle between the scattered particle direction and the blade surface which allowed travel through the final collimator is about 10^{-3} deg. As shown in the Figure 4.2, it is hard to find scattered particles which can pass through the copper aperture. In some other experiments, where the distance between two collimators is small, the maximum angle would be larger, for example the maximum angle is about 0.1 degree if the distance is several millimeters.

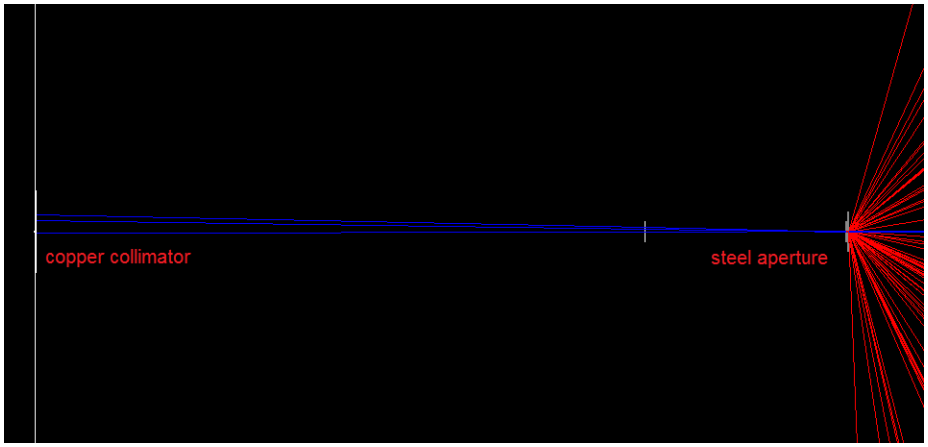

Figure 4.2: Rare scattered particles from the steel aperture could reach the target in the ideal conditions. To clearly demonstrate scattering, the primary particles which passed through the apertures without interactions were not plotted. Blue line: protons; Red line: delta rays; Grey: steel blades. The distance between the two apertures is not in the same scale with the apertures.

Figure 4.3 shows the scattered particles spread out quickly after interacted with the steel aperture blades, and it is hard to see any scattered particles in the 50 μm X 50 μm square around the primary beam when the distance from the steel aperture is larger than 30 mm. So all primary particles will travel through the second aperture in ideal conditions cleanly if the distance between the two apertures is not too small.

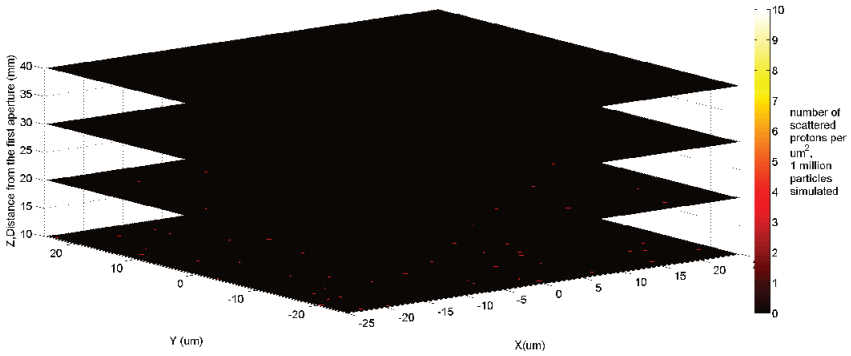

Figure 4.3: Scattering from the steel aperture under ideal conditions. The color represents scattered particle density at different distance from 10 mm to 40 mm when 1 million primary particles in the main beam. Primary particle: 3 MeV protons

Simulation results showed that the probability of one primary particles to be scattered and directly irradiate a non-targeted cells is less than 10^{-6} in the ideal conditions.

4.1.2 Steel collimator shape effects

In the real experimental setup, neither are the collimator blades ideal rectangles nor is the blade surface parallel to the radiation direction. The roughness of the surface finish and the angle between the surface and the radiation beam are factors that can increase scattering from the collimator.

The angle between the surface of the blade and the beam direction creates a small zone on the edge (Figure 4.4 shows the zone width is d). When particles incident on the edge within the zone, most of them will be transmitted through the blade. The width of the zone only depends on the CSDA range of charged particles in the material and the angle between the blade edge and the beam direction. The width of the zone is about 0.2 μm for 3 MeV protons in a steel collimator if the angle α in Figure 4.4 is 1 degree. Comparing with the ideal condition, the small tilt angle

hugely increased the probabilities of primary particles to be scattered out of the aperture blade. Although the particles impinged on the zone would travel through the steel blade, a small fraction of the reduced energy particles would travel within small scattering angle with the initial beam direction and go through the second aperture.

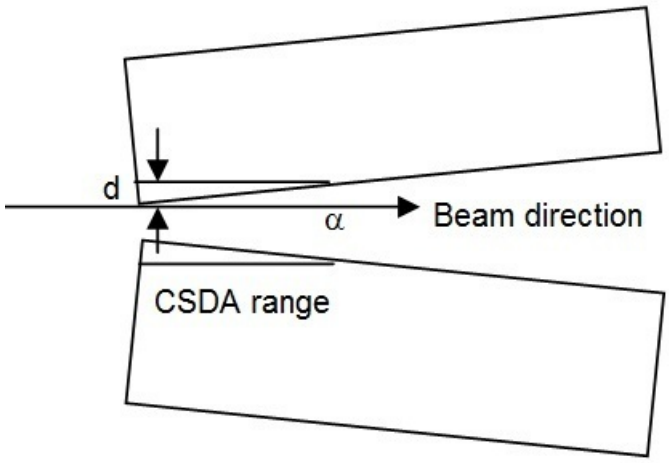

Figure 4.4: The angle between the steel blade edge and beam direction cause a transverse zone.

Due to cutting tools, environmental conditions, and the material itself, all machining processes will produce some roughness on the surface. There are several measurements used to describe the surface roughness properties:

Ra: The average the arithmetic mean of the absolute departures of a roughness profile from the mean line of the measurement. Usually surface finish level mean Ra.

Rp: Highest peak height along the assessment length.

Rv: Deepest valley depth along the assessment length.

R(p+v): Rp + Rv.

Generally, for abrasive finished surface, the surface finish Ra falls in 0.2 to 1.0 μm. Rp + Rv value, however, is much larger, about 1.2 to 5.0 μm. So the variation of the surface peaks and valleys on a abrasive finished aperture blade is the same order as the 3 μm gap between the two aperture blades. The small peaks of the surface would significantly increase scattering from the blade edge.

After interaction of the charged particles with the small peaks on the rough surface of the steel collimator, the direction and energy of a charged particle will be changed slightly due to the small interaction length. The surface roughness slightly enhances the probability of scattered particles traveling through the steel aperture and reaching the copper collimator, resulting in an increased percentage of partial energy particles reaching the target. Depending on the alignment and the direction of scattered particles, the partial energy scattered particles either directly irradiated the target cell or scattered again on the copper collimator. The particles that directly reached the target tissue would change the energy deposition properties, while the particles interacting with the edge of the copper aperture would were either be absorbed by the collimator or scattered again and hit cells surrounding the target. Lower energy particles reaching the targeted cell and changing energy deposition is important when exact number of particles is required to be delivered to the targeted cell. It will significantly change the energy deposition when only a few particles are desired in one irradiation. But it is negligible in the Loma linda/TAMU experiment as the number of particles to one cell nucleus is a relatively large number, following a Poisson distribution. So the energy deposition varies following Poisson distribution even if every particle deposits the same amount energy.

The second situation, in which the scattered particles irradiated non-targeted

cells, is a more important issue in the bystander effects research. The probability of scattered particles transversing surrounding cells should be controlled to a very low level to exclude the possibility that the radiation effects in surrounding cells are induced by scattered radiations, rather than the radiation bystander effects. Furthermore, the most important purpose of using a charged particle microbeam to irradiated a single cell in bystander effects research is to distinguish the directly irradiated cells and non-irradiated cells, in order to study the biological differences in directly irradiated and unirradiated bystander cells, signal transfer and linkage between cells, etc. So knowing the probability of surrounding cells being irradiated is important in the bystander effects research. However, it is hard to get the exact number through simulation since the roughness of the steel aperture surface is hard to measure and to model and the scattering is sensitive to the tilt angle of the surface and the peaks on the surface near the edge where it is closest to the aperture center-line. In the following paragraphs, the simulation results and several models are discussed.

4.1.2.1 Surface Models

According the surface roughness level, a similar simple model was built with triangular peaks on the surface with average height of 0.2 μm to represent a surface finish level of Ra = 0.2 μm. The height of the peaks is randomly generated with a half normal distribution (The positive half of the normal distribution curve), and the largest is around 0.6 μm which is close to the maximum peak value on the real surface with Ra = 0.2 μm (Appendix A Table A.1). In radiation experiments, the scattering mainly comes from the tinny peaks on the surface, the valleys play important roles only when the thickness of the aperture blade is similar to the range of ionizing radiations and the valleys reslut some primary particles not being stopped in the

blade. The model which could represent the real surface in our setup as shown in the Figures 4.5.

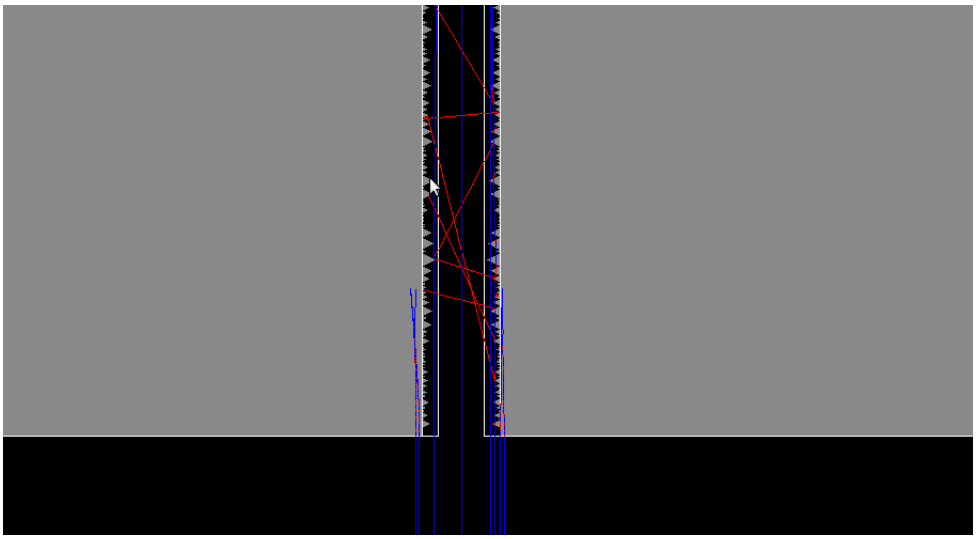

Figure 4.5: The simple surface roughness models just contains small peaks on the surface without valleys to simply represent the rough surface. The height and base length of peaks were generated randomly and the number of the peaks also varies to fill the whole edge. The figure shows Ra = 0.2 μm and Rp = 0.6 μm.

The peaks on the surface largely increased the probability of scattering with small direction change. Figure 4.6 and 4.7 show the scattered particle density around the main radiation beam at different distances after they pass the steel aperture, with an ideal shape and roughness surface model described above respectively. In both figures, the the angle between the steel aperture blade surface and the direction of the beam is 1 degree.

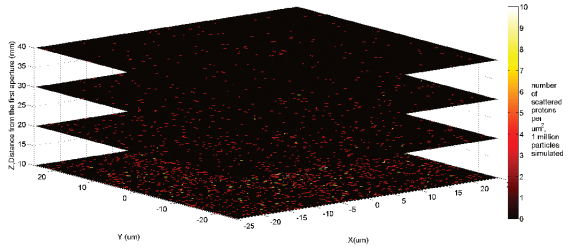

Figure 4.6: Scattering particles at different distance from the target tissues for ideal shape collimator. A 25 μm X 25 μm area is ploted. The color in the figure depends on the number of scattering particles per square micrometer when 1 million primary particles travel through the copper collimator hole. The results represent an ideal shape steel collimator and the angle of steel collimator edge to the radiation beam is 1 degree.

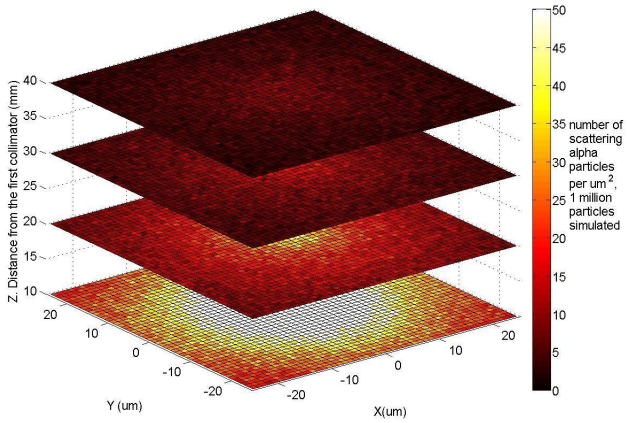

Figure 4.7: Scattering particles at different distance from the targeted tissues for real steel collimators. A 25 μm X 25 μm area is ploted. The color in the figure depends on the number of scattering particles per square micrometer when 1 million primary particles can travel through the copper collimator hole. The collimator model is shown in the Figure 4.5 and the angle of steel collimator edge to the radiation beam is 1 degree.

For the ideal rectangular shape steel apertures, particles scattered from the in-

teractions of the primary particle with the edge of the aperture blades is very rare, even if the angle α, between the blade surface and beam direction, is 1 degree. The scattered particle flux is about several particles per μm^2 per 1 million primary particles at the surface 10 mm away from the steel aperture in vacuum, and decreases quickly with the distance from the steel aperture. It is difficult to see the scattered particles when the distance from the first aperture is larger than 20 mm. The simulation results from our rough surface model (Ra = 0.26 μm, Rp=0.8578 μm), show scattering is more obvious compared to the ideal shape. The scattered particle flux is about 100 per μm^2 per 1 million primary particles at the 10 mm away from the steel aperture and is about 20 at the surface which is about 30 mm from the target. It also decreases quickly with the distance.

Table 4.1 lists the number of scattered particles that could pass through the copper aperture for different aperture distances from 10 mm to 40 mm per 1 million primary particles and the percentage of the partial energy particle to the total number of particles traveling through the apertures. The result for ideal shape and rough surface model were compared. In both configurations, α, the angle between the beam direction and steel blade surface, is 1 degree. For ideal conditions (α = 1 deg) the scattered particle percentage in the main beam is only 0.0019%, the percentage is even lower at greater distances. For the rough surface models, the percentage drops from 1.2% to 0.17% when the distance between the two apertures increases from 10 mm to 40 mm.

The energy distribution of the scattered particles changed slightly with the distance from the steel aperture (Figure 4.8). Low energy particle probability decreases with larger distance, but the energy of most scattered particles is close to the full

Table 4.1: Total number of non-full energy primary particles within 5 μm diameter of the center

Model		Distance from the steel aperture			
		40 mm	30 mm	20 mm	10 mm
Rough edge	Number	1724	2422	4229	12412
	Percent(%)	0.17	0.24	0.42	1.2
Ideal edge	Number	0.75	0.75	1.5	18.5
($\alpha = 1$ deg)	Percent(%)	0.0001	0.0001	0.0002	0.0019

energy particles. The fraction of scattered particles for which the energy is less than 90% of full energy is less than 5%.

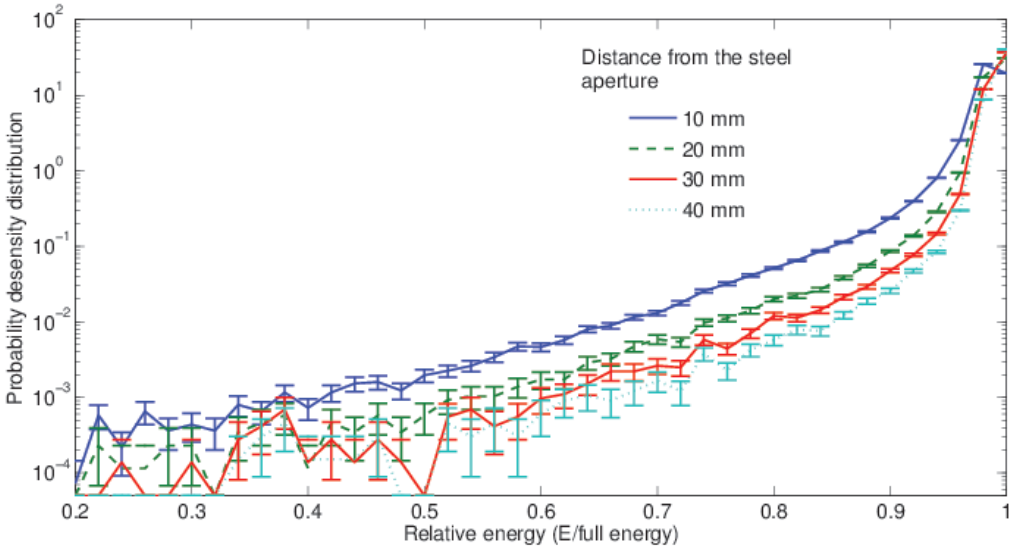

Figure 4.8: Energy spectrum of scattered particles at different distances from the steel aperture from 10 mm to 40 mm. A 25 μm X 25 μm area around the main beam was scored. Errorbars show one standard deviation.

Based on the results, we concluded that both the tilt angle of the steel blade and the surface roughness increase scattering to the main beam, but the surface

finish contribute much more to the scattering than the tilt angle. The 1 degree tilt angle fraction the non-full energy percentage in the main beam from negligible to 0.0019% at the surface 10 mm away from the aperture, however with the roughness level of Ra= 0.2 μm, the probability at the same distance is 1.2%. Second, with larger distance between the two apertures, the scattered particles in the main beam decreases quickly. The scattered particle flux decrease approximately proportional to $1/d^2$, where d is the distance from the steel aperture. So the scattering from the first aperture only affects the beam quility for single aperture system or when the distance between the two apertures is small. To improve the collimation system performance, larger distance between the two apertures is preferred, but increasing the distance between the two apertures makes it difficult to align the apertures.

In the Loma Linda/TAMU experimental setting, the distance between the two apertures is about 30 cm. The large distance makes the probability that a scattered particle from the first aperture passing through the second aperture extremly small. Results show that the number is less than 5 per million primary particles.

4.1.3 Copper collimator effects

The copper aperture is the last substantial shield before charged particles reach the target cell or nucleus, and serves to block scattered particles that have not cleanly passed the first aperture. At the same time, the particles scattered from the copper collimator would directly irradiate the target and surrounding cells. To minimize the scattering from the copper aperture and block as many scattered particles from first aperture as possible, the aperture plate should be thicker than the CSDA range of full energy particles and the aperture should be larger than the first aperture. Compared to the scattering from the steel aperture, scattering from the copper aperture is more important to the results of the biological experiment as there is no further shield after

particle travels through it.

As discussed in section 4.1.1, charged particles will travel through the copper aperture hole without any interactions if collimator shape, dimensions and the alignment are ideal. If the apertures are not ideally aligned or the diameter of the second aperture is too small, the radiation beam could impinge on the edge of the aperture, inducing particle scattering. In addition, the scattered particles from the first aperture could also be scattered again and travel through the laser hole to reach target cells, but the probability is very low in the Loma Linda/TAMU experiment because of the large distance between the two apertures. In some other experiments ([18]), when the two apertures were not very far apart, the probability, however, is not negligible.

When particles impact on the edge of the copper aperture, whether due to improper alignment or smaller size of the second aperture, the inner wall geometry of the laser hole would affect the scattering a lot. As discussed in the Model section, laser drilled holes usually have poor inner wall surface finish and smaller entrance than exit, which increases the scattering and reduces the full energy particle percentage. The inner wall surface roughness depends on the laser properties and environmental conditions when drilling. While the ratio of the entrance diameter to the exit diameter depends on the laser used for drilling and also the thickness of the copper. With thinner copper foil the diameter of the exit is closer to the diameter of the entrance. So the copper collimator should be selected as thin as possible, as long as it can stop the full energy particles, in order to reduce the scattering from the inner wall of the laser drilled hole.

In addition, the zone around the hole, which is about 1 μm wide, is also affected by the heat of the laser beam, reducing the thickness of the copper shielding around the collimator. In most experiments with microbeam facilities, this effect will be

negligible, but if the thickness of the copper aperture plate is close the the range of full energy particles, the reduced thickness could induce additional low energy scattering to the target or surrounding cells.

In the Loma Linda/TAMU experiment, the copper aperture is a 25.4 μm (0.001 inch) thickness copper foil with a 5 μm-diameter laser drilled hole in the center. The projected range of a 3 MeV proton in copper is about 22 μm, so the copper collimator is thick enough to block all scattered and un-aligned particles. The steel aperture is a 3 μm by 3 μm square, so the diameter of the laser hole is large enough for the square radiation beam.

4.1.3.1 Inner wall model

The wall morphology of laser drilled holes has been investigated by slicing the holes along their length in several studies. The morphology is quite different for different materials depending on the metal properties. Weck *et al.* [19] studied the inner wall structure of high aspect ratio holes in copper. Regular ripples were seen on the wall of the holes when they were machined in air with laser pulse length between 150 fs and 1 ps. For shorter pulse lengths, ripple structures were reduced and smoother sections are present. When the holes were drilled in vacuum, the surface appears as if liquid droplets condensed on the surface instead of the ripple structure. The size of these features was relatively constant in their research, about 0.2 μm.

In the mathematical models, small cylindrical sections were used to represent the ripples on the surface of the laser drilled hole as shown in Figure 4.9. To fit the small sections on the inner surface of the hole, the outer radius is the same as the radius of the hole at the position where the cylindrical sections were located. The thickness, which is the outer radius minus inner radius, of the cylindrical sections represents

the height of the ripples. In the simulation, random numbers of the thickness with a Gaussian distribution were generated to represent the uncertainty of the ripple heights. The average thickness was set to 0.14 μm, and the standard deviation was 0.02 μm. So 95% of the model ripples height falls between 0.1 and 0.18 μm, and about 2% falls between 0.18 and 0.2 μm. To prevent the possibilities of generating ripple height larger than 0.2 μm, for which the probability is 0.13%, an upper limit of 0.2 μm was set. The arc length of the cylindrical sections was also randomly generated and the average value is 0.2 μm. Data are shown in Appendix A Table A.2 and Table A.4.

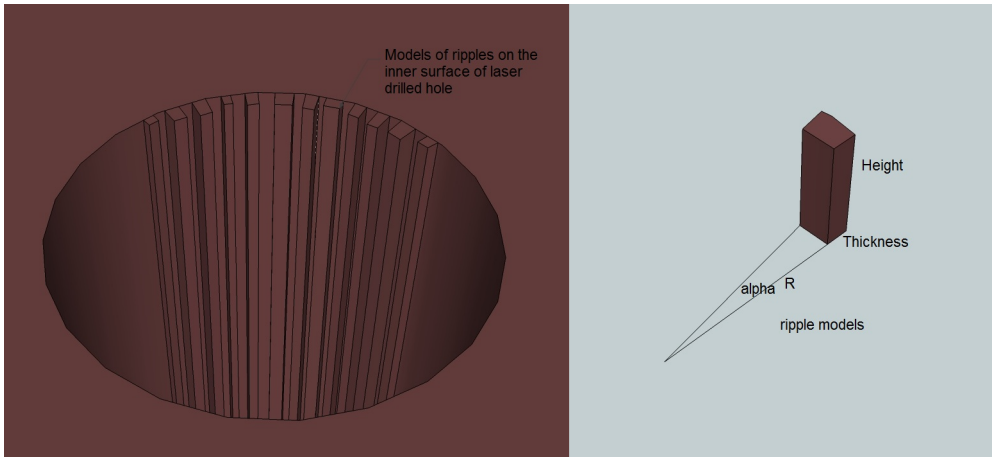

Figure 4.9: Computer models of the ripples on the inner surface of the laser drilled hole. Left figure: overview of the models on the inner wall; Right: cylinder section used to represent the ripple.

Triangular, rectangular, and sphere shapes were used to build the liquid droplets on the surface, especially for the holes drilled in vacuum. Setting similar to those used for the cylindrical sections representing ripples were used for the droplet dimensions.

4.1.3.2 Scattering on the inner wall

To study the effects of the laser hole morphology on the scattering, several different diameters of the laser whole model were simulated, and the results comparing with ideal condition copper aperture are shown in Table 4.2. In the simulations, a 3 μm by 3 μm square aperture was used, and its model was described in the steel aperture section. The diameters shown in the table were the exit diameters of the laser hole, which is mounted to be the entrance side for the radiation beam to reduce scattering. For the 5.0 and 4.4 μm diameter configurations, the copper aperture is clearly larger than the first aperture, so the full energy particle fraction is high and the probabilities of the non-targeted cells being irradiated were low, the results for the two distinct settings are different because some of the main beam particle may hit the small ripples in the 4.4 μm diameter aperture. If the dimension of the second aperture is clearly smaller than the first aperture, for example, 2.4 μm shown in the table, the scattering is significant on the small ripples, with only 51% of full energy particles and the probability of having one surrounding cell nucleus to be irradiated is 3%.

The scattering is more obvious if the diameter of the copper aperture decreases. So in the collimator design, it is important to make sure the size of the second aperture is larger than the first one. Considering the rough surface finish, the dimension of the second aperture is larger than expected.

4.1.4 Alignment

For mechanical collimatiors, alignment of the apertures is the most important task. Nearly perfect alignment is necessary to reduce scattering in the inner wall of the apertures and maximize the full energy particle percentage. The small diameter of the apertures makes alignment a delicate task in most collimated microbeam

Table 4.2: Probabilities that non-target cell nuclei are irradiated for different the copper aperture diameter and different models

Aperture diameter (μm)		5.0	4.3	4.0	3.5	3.0	2.5
P(>0.9E)	ideal	1.0	1.0	0.99	0.96	0.88	0.73
	ripple	1.0	0.99	0.96	0.90	0.78	0.49
P1(%)	ideal	0	0.001	0.001	0.005	0.03	0.05
	ripple	0.0004	0.002	0.005	0.009	0.05	0.1
P25(%)	ideal	0	0.03	0.03	0.1	0.7	1
	ripple	0.01	0.05	0.1	0.2	1	3

P(>0.9E): fraction of particles with energy greater than 90% of full energy.
P1: Probabilities of non-target cell nucleus are irradiated,
if one primary particle hits the target nucleus.
P25: Probabilities of non-target cell nucleus are irradiated,
if 25 primary particles hit the target nucleus.
ideal: simulation with ideal shape of copper aperture.
ripple: simulation with the inner surface models.

facilities.

If the two apertures are well aligned, the scattered and partial energy particles are negligible even though the surface of the first aperture is rough, as long as the the minimum diameter of the second aperture is larger than the diameter of the first. Simulation results shows that the fraction of full energy particles is more than 99% for a well aligned system, and the non-full energy particles are the scattered particles from the edge of the tiny rough peaks on the steel aperture edge. If the two apertures are not suitable aligned, primary particles have a chance to hit the rough inner wall of the second aperture, reducing the full energy particle percentage and increasing the probability of scattering to surrounding tissues.

Several simulations were conducted to study the relationship of scattering and the offset distance of center axis of the two apertures (Figure 4.10). All results were based on the models described in the steel aperture and copper aperture sections. The steel aperture is a 3 μm by 3 μm square with 1 degree tilt angle between the

beam direction and inner blade surface. The diameter of the copper aperture was set to 5 μm with ripple models on the inner wall surface.

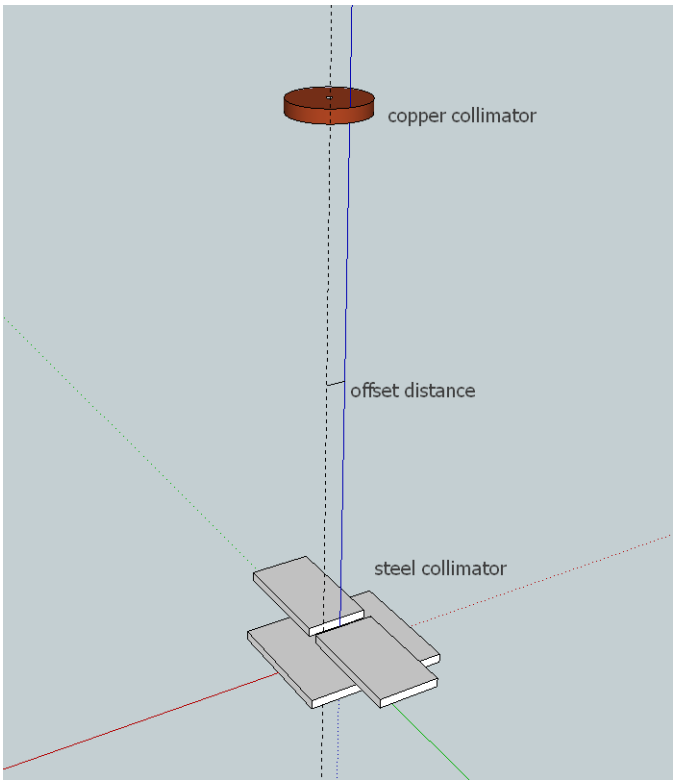

Figure 4.10: Distance of the two apertures center axis in poor alignment conditions. The scales in the different parts may be different.

Table 4.3 shows the relationship of full energy particles that irradiate the target cell nucleus. If the offset is less than 0.35 μm, the scattering is negligible and the beam is as good as ideally aligned of the two apertures. For offset distance larger than 0.5 μm, the scattering increases quickly. The larger size of the second aperture allows some alignment errors of the two apertures.

Figure 4.11 illustrates the energy spectrum of particles scattered from the copper aperture. Unlike the energy distributions of the scattered particles from the steel

Table 4.3: Full energy particles percentage to the target for different alignment conditions

Offset Distance (μm)	Full energy particles(%)
<0.35	100
0.5	99.8
1.0	97
1.5	89
2.0	83

aperture, there are more lower energy particles after scattering from the laser hole. The differences are caused by the large scattering angle of low energy particles. Due to the large distance between the two apertures and the thickness of the steel aperture blades, scattered particles with large angles are either absorbed by the collimator or scattered out. However, the distance between the target and the copper aperture is only several micrometers, so all scattered particles, if traveling through the laser hole, will irradiate the target. In addition, the small thickness of the copper foil sheet, which is only a little larger than the CSDA range of the primary particles, allows more scattered particles travel through the aperture.

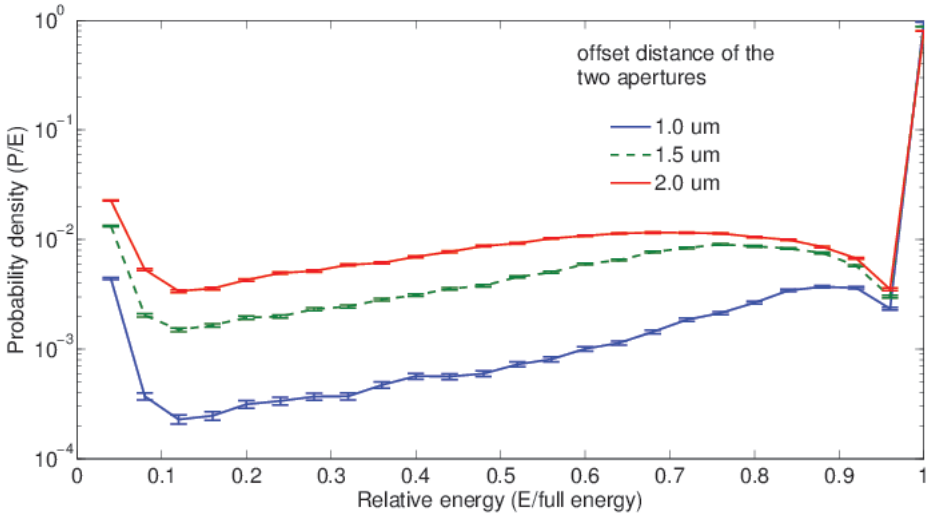

Figure 4.11: Partical energy distributions in different alignment conditions, when the offset distance between the two apertures is 1.0,1.5 and 2.0 μm. 1 million primary particles in the main beam were simulated. Errorbars show one standard deviation.

Table 4.4 shows the probability that a non-targeted cell nucleus would be irradiated under different alignment conditions comparing the ideal copper aperture and our computer model. If the target nucleus is irradiated by 25 primary particle per irradiation, the possibility that a non-targeted cell nucleus is irradiated is about 3% estimated for our computer modelof a typical aperture, and 2.2% for an ideal copper aperture. The rough inner wall surface of the copper aperture increases the probability of scattering to other nuclei, but the effect is not very significant. However the fraction of the low energy scattered particles reaching the target tissue, which would affects the absorbed dose in the targets, is much larger using the rough surface aperturemodel.

Table 4.4: Probabilities of non-target cell nuclei being irradiated for different alignment conditions

Offset distance (μm)		0	0.5	1.0	1.5	2
P(>0.9E)	ideal	1	1	0.98	0.96	0.93
	ripple	1	1	0.97	0.89	0.83
P1(%)	ideal	0	0.0004	0.008	0.05	0.09
	ripple	0.0007	0.0004	0.01	0.06	0.1
P25(%)	ideal	0	0.01	0.2	1	2
	ripple	0.06	0.01	0.3	2	3

P(>0.9E): fraction of particles less than 90% of full energy.
P1: Probabilities of non-target cell nucleus are irradiated, if one primary particle hits the target nucleus.
P25: Probabilities of non-target cell nucleus are irradiated, if 25 primary particles hit the target nucleus.

4.1.5 Minimun beam size the mechanical collimator can create

In some radiation biological effectiveness studies, only parts of the DNA are desired to be irradiated rather than the whole cell nucleus. Thus, sub-micrometer precision is required to deliver the charged particles to the experiment sites. However, the scattering increases when the diameter of the collimator aperture decreases. And the scattering in the plastic sample plate and the target tissue makes the beam spread out. The minimum diameter of the mechanical collimation charged particle beam is restricted by the collimator, scattering in tissue, and mechinical properties of the collimator. The particle usage efficiency is also a limitation to the particle beam, if the beam is too thin the irradiation time would be extended for enough dose, as a result the worm movement during irradiation time would enlarge the uncertainty.

4.1.5.1 Scattering for different diameter

The surface roughness level of the collimator inner wall contributes a lot to the main beam scattering. The scattering effects becomes dominant when the diameter

is smaller. Table 4.5 shows the primary particle energy distribution for different copper aperture diameters. Model parameters are shown in Appendix A Table A.3. In the simulation, the steel aperture is set to 0.4 μm. Although the diameter of the laser hole in the copper aperture is larger than the diameter of the steel aperture for the 0.6 μm and 0.8 μm diameter setting, the ripples and peaks on the inner wall of the laser drilled hole have a chance to block some particles. For the 0.6 μm diameter copper aperture, only 68.7% of particles have energy larger than 90% of the full energy. For the 1.4μm diameter laser hole, the full energy particles are only 99.7% due to the scattering in the thin rough peaks in the steel collimator and their energy is only several keV shy of the full energy, so their energy is considered to be full energy particles.

Table 4.5: Full energy particle percentage to the target at different copper aperture diameters with the steel aperture set at 0.4 X 0.4 μm

Diameter (μm)	0.3	0.6	0.8	1.4
minimum Diameter (μm)	0.16	0.35	0.5	1
Full energy percentage (%)	20	37	83	99.7
Larger than 90% of full E (%)	52	69	97	100

Although the full energy particle percentage is low for small laser hole diameters, the probability of the non-targeted cell nucleus being irradiated is relatively low and the probability of the surrounding objects being irradiated is negligible if only one or two particles are delivered to the targeted cell nucleus. But in the Loma Linda/TAMU experiments, about 25 primary particles are delivered to the target cites per irradiation, the probability of the surrounding cell nucleus is irradiated is much larger as shown in Table 4.6.

Table 4.6: Probability of a surrounding cell nucleus being irradiated when intestine cell nucleus 6d is targeted using a 0.4 X 0.4 μm steel aperture and the listed copper apertures

Diameter (μm)	0.3	0.6	0.8	1.4
4v (%)	0.02			
5d (%)	0.005			
6v (%)	0.1	0.09	0.01	
6d (%, the target)	100	100	100	100
7d (%)	0.03	0.009		
Total for non-target(%)	0.2	0.100	0.013	
Total for 25 primary particles(%)	4.52	2.48	0.33	

The smaller diameter of the collimators requires better alignment precision to minumize the scattering in the second collimator. Table 4.7 shows effects of the offset distance between the two aperture center axis on the scattering and full energy percentage for different copper aperture diameter. The steel aperture setting is the same for the two simulations, 0.4 μm square. The smallest diameter of the 0.8 μm diameter second collimator setting is similar to the size of the first diameter, so a small offset of the two collimator center would result in the part of the main radiation beam hitting on the edge of the laser hole. But for the larger diameter second collimator setting, the 1.0 μm minimum diameter is still much larger than the first collimater diameter, so providing a large allowance for alignment error.

Table 4.7: Probability of the surrounding cell nucleus are irradiated

Diameter (μm)	0.8 (minimum 0.5)			1.4 (minimum 1.0)			
Offset of collimators (μm)	0	0.1	0.3	0	0.1	0.3	0.5
Full Energy (%)	84	76	60	100	100	95	68
P(>90% of full Energy)	97	93	81	100	100	99	88
P1(%)	0.01	0.02	0.08	0	0	0	0.1
P25(%)	0.3	0.4	2	0	0	0	3

The adjustable steel collimator can produce smaller diameter beams, but the limitation is the laser drilled holes in the copper collimator due to their natural disadvantage that laser drilling is not capable of making high aspect ratio holes. Also, holes produced in this way are tapered and have poor surface finish, which will increase scattering and degrade the energy spectrum.

4.1.5.2 Scattering in the tissue

Because of the scattering, identical charged particles do not follow the same path in tissue, nor are the paths straight, especially for light particles. Multiple scattering in the matter spreads the initial parallel beam of charged particles into a conical angular distribution (Figure 4.12). The magnitudes of direction and range straggling vary depending on the energy, mass, and particle charge. Since light particles (protons) are more easily scattered than heavier particles (alpha particles), their energy would be deposited in a relatively large volume due to the direction straggling. Figure 4.12 shows the scattering of a 3 MeV proton beam in water. The primary particle beam is 0 diameter when entering the phantom (red color), but at 60 micrometer depth the beam spreads out to about 2 μm in diameter.

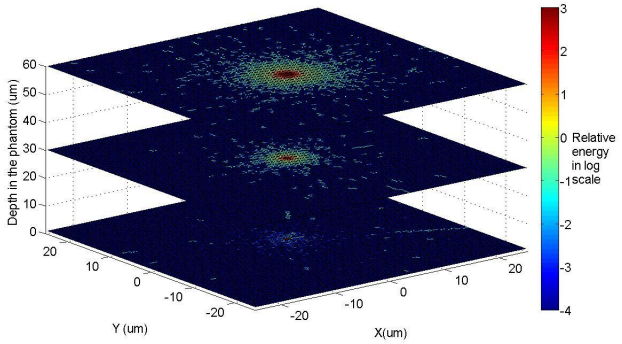

Figure 4.12: The spreading of 3 MeV proton beam at different depths in water. All particles enters the water phantom at the same position and identical direction.

Considering that the detector for single particle applications is about 10 μm, and is usually mounted between the second aperture and the sample plate, the total thickness of matter the radiation beam has to travel through before reaching targeted cell nucleus is around 20-60 μm. The diameter of the beam is then about 0.3 to 2 μm larger than the original beam size. This spreading out makes producing a vary small radiation beam meaningless.

The scattering in the phantom could contribute to the scattering to non-targeted cell nuclei. Table 4.8 shows the probabilities of non-targeted cell nuclei to be irradiated for different cell nuclei depths in phantom. Scattered particles from the copper aperture and in the phantom contribute to the probabilities of surrounding cells to be irradiated. Most scattered particles have only small scattered angles, so the probabilities for the scattered particle reaching a surrounding cell is small if the worm is located at the surface of the water phantom. But if the worm is located too deep in the phantom, the range of low energy charged particles is too short to irradiate a surrounding nucleus.

Worms are usually located near the surface of the water phantom to easily align the targeted nucleus and the aperture, so the detector which is usually mounted between the sample holder and the collimator will increase the probability of scattered particles irradiating non-targeted cell nuclei when it provides information of the number of particles reaching the target.

Table 4.8: Probabilities of the surrounding cell nuclei are irradiated for different target cell nuclei depths in phantom

Depth (μm)	10	20	30	40	50	60
P1(%)	0.17	0.22	0.33	0.37	0.35	0.26
P25(%)	4.2	5.4	7.9	8.9	8.5	6.5

Results based on the rough steel aperture and copper aperture model.
To evaluate scattering, the offset distance between two apertures is 2 μm.

4.2 Energy deposition

A charged particle, being surrounded by its Coulomb electric force field, loses its kinetic energy by interacting with one or more electrons or with the nucleus of practically every atom it passes. Delta rays are ejected from the atom when a hard collision occurs between an atomic electron and the charged particle. Due to the range of the scattered delta rays, the kinetic energy of charged particles is deposited in a larger volume than that occupied by the original beam.

For a hadron particle with several MeV per nucleon, the continuous slowing down approximation (CSDA) range in water of the most energetic secondary electrons is around 100 nm. The energy deposition for a beam of 3 MeV protons in water is shown in Figure 4.12. For 3 MeV protons, the most energetic secondary electron is about 3 keV [22], for which the CSDA range in water is about 300 nm. The figure shows that most kinetic energy is deposited in a very short range, the doses dropped quickly outside of the main beam (yellow color shows dose is only 1/1000 of the dose indicated by red color).

The energy deposition in the target and surrounding cells is the key issue concerning biologists conducting bystander effect studies. For a rough estimation, the stopping power/LET data can be used. But it is far from precise, as the stopping power varies when a particle travels through a medium, especially when the it reaches

the end of its range. The path length in a cell/cell nucleus is different depending on the position a particle entering the cell nucleus, particle scattering and beam straggling. More detailed information about energy deposition in a specific cell and cell nucleus can be obtained through target simulation and Monte Carlo calculation.

The average energy deposition in the worms can be estimated using the stopping power of the source particles. The stopping power of a particle in a material is defined as the average energy loss per unit path length at the point in the specified the material, as a result of Coulomb interactions with electrons and with atomic nuclei[23, 22]. The stopping power is subdivided into collision stopping power and radiative stopping power, when considering the fate of the energy lost by the charged particle. The former is the rate of energy loss resulting from the sum of the soft and hard collisions, which are conventionally referred to as collision interactions. Radiative stopping power is that due to radiative interactions, which are almost exclusively bremsstrahlung production.

For protons and alpha particles, the predominant contribution to the total stopping power comes from the electronic stopping power (collision stopping power), due to inelastic collisions with electrons. A smaller contribution comes from the nuclear stopping power, due to elastic Coulomb collisions in which recoil energy is imparted to atoms. The radiation stopping is very low for heavy particles at low energy.

The nuclear stopping power is important only at very low energies. For example, in water, the nuclear stopping power contributes more than one percent to total stopping power only at energies below 20 keV for protons and 150 keV for alpha particles. The radiative stopping power (due to emission of bremsstrahlung) which is important for electrons, is negligibly small for protons or alpha particles, because it is inversely proportional to the square of the mass of the charged particle.

The collision stopping power strongly depends on the velocity of the particle. The

collision stopping power increase rapidly as the particle velocity decreases (until the particle's effective charge starts to decrease). The steep rise in stopping power for the low energy range largely accounts for the Bragg Peak observed in the absorbed dose near the end of a charged particle's path.

Linear energy transfer (LET) is the energy transferred per unit length of the track. The special unit usually used for this quantity is kiloelectron volt per micron (keV/um) of unit density material. The linear energy transfer of a charged particle in a medium is the quotient of dE/dL, where dE is the average energy lost by a charged particle of specified energy in traversing a distance of dL. That is, $LET = dE/dL$, the stopping power.

4.2.1 Energy deposition sensitivity with the position

The CSDA range of 3 MeV protons in water is about 200 μm, which is much larger than the diameter of the worm body. When the particles traverse through the targets, the LET increases as the particle energy decreases. So the dose to the target cell/nucleus is sensitive to their position in the radiation target phantom. Figure 4.13 shows Monte Carlo results for the relative dose at different depth of the target after running large numbers of particles. The dose at the depth of 50 μm is about 30% larger than the dose at the 10 μm depth. The relationship of dose to the target and the depths of the target in the water phantom makes the precise dosimetry difficult in the experiment. The depth of the target nucleus depends on the thickness of plastic plate, scintillation detector and also its position in the worm body. So the dose evaluation depends on the experimental setup. The intestine cell rings have a 180 degree rotation from ring I to VIII, resulting the expected dose to the nucleus differing in the same experimental setup.

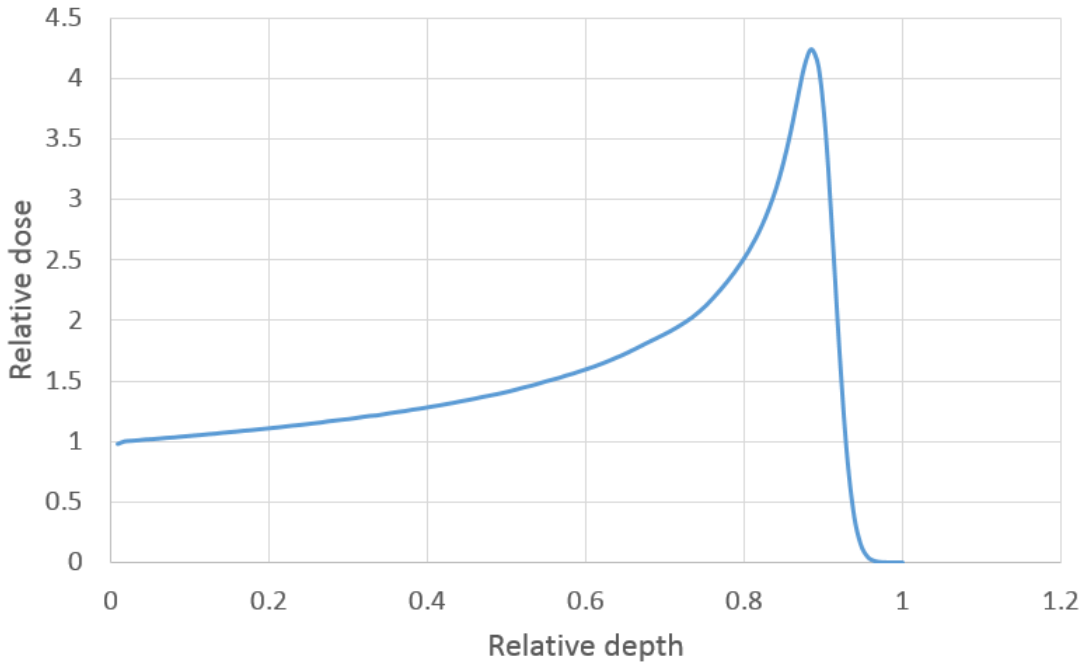

Figure 4.13: The dose of 3 MeV protons in water phantom at different depth of the phantom. Results based on Monte Carlo simulation of a large number of particles.

For heavier charged particles, alpha particles for example, LET increases faster near the end of the track than it does for protons. So precise dosimetry of heavier charged particles in the small worm body is more challenging than for protons.

Another issue affecting dosimetry is the number of particles to the target cell nucleus. In the corresponding experiment, there were about 25 protons delivered to the target nucleus per irradiation. To control the number of particles delivered to the target, the target nucleus were irradiated for a specific time by operating the shutter locating under the steel collimator. During the irradiation interval, a large number of source particles is generated from the accelerator but only a small random number of particles could reach the target nucleus, because the small diameter of the collimator and the probability that a single primary particles can travel through

the collimator is very low. The number of particles delivered to the target follows a Poisson distribution, with an expectation of 25 (Fig 4.14). The simulation reported here followed the same process as the experiment. A large number of source particles were generated randomly distributed in a broadbeam to simulate fixed irradiation time interval. The number is calculated by the probability that a particle travels through the collimator and the expectation value of particles required to be delivered to the target nucleus. Fig 4.14 shows the distribution of the number of primary particles transverses the target nucleus and compares the distribution with Poisson and Gaussian distribution. The distribution of particle numbers delivered to the target is close to Gaussian, with the average of 25, and standard deviation of 5. The particle numbers have a probability of 65% to fall in between 20 to 30 , and 95% to fall in between 15 to 40. The probability of the number below 5 is negligible as it is less than 0.15%.

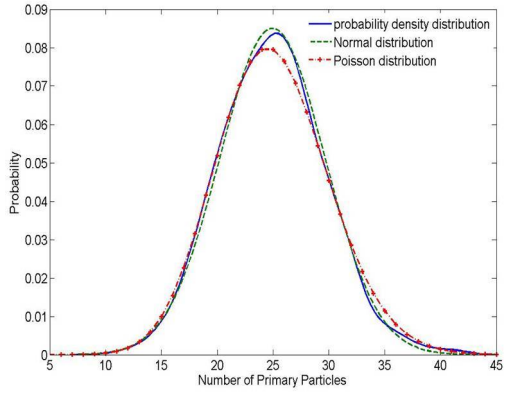

Figure 4.14: Results of Monte Carlo calculation of the number of particles delivered to the target cell nucleus, when the fluence at the first aperture was set to produce an expectation of 25. the result is a Poisson distribution. The large expectation values makes the distribution close to Gaussian

Since the number of parimary particles delivered to the target is randomly distributed, total energy deposition in one irradiation (averge 25 primary particle in the simulation) to the target nucleus is also close to a normal distribution, and the average depends on the depth of the target nucleus in the phantom (Figure 4.15). In the simulation, the diameter of the target nucleus was set to 3.3 μm, which is the average of the L1 stage intestine cell nucleus diameter [20]. To get low variation of the energy deposition spectrum, 1 million protons were simulated. The collimator model using the rough surface aperture model with a 3 μm square steel aperture and 5 μm copper aperture, and they were precisely aligned. The expected energy deposition in the target nucleus is larger if it is located in deeper location in the water phantom. The average energy deposition is about twice when the target nucleus is located 60 μm depth in the phantom of the energy deposition when it is located near the surface of the phantom (0 μm in Figure 4.15).

In addition, the variation of the energy deposition is much larger when the target nucleus is in a deeper location due to the energy struggling. The 3 μm square beam does not fit into the 3.3 mum diameter cell nucleus, not all particles delivered by the microbeam facility irradiate the target cell nucleus. The possibility that some particles travel through the aperture are not delivered to the target nucleus caused the small peak beside the main peak on the energy deposition spectrum curve (0 μm in Figure 4.15).

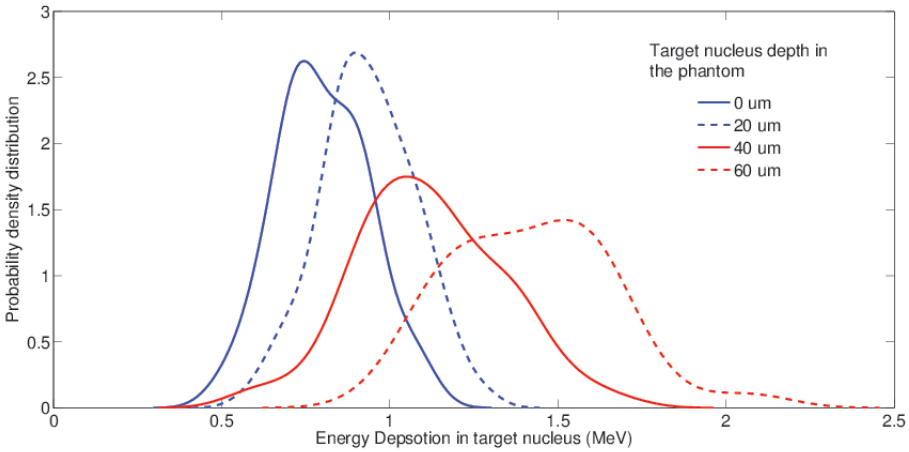

Figure 4.15: Monte Carlo calculated dose to the target nucleus follows Gaussian distribution, and depends on the depth in the phantom. Energy deposition in the deeper nuclei is a larger than the shallow ones because of bragg-peak effect. Nuclei are assumed to be spheres 3.3 μm in diameter. 1 millition 3 MeV protons simulated.

4.2.2 Alignment of the target and collimators

The small diameter of the radiation beam requires precise alignment of the target cell nucleus and collimator in order for the planed dose to be delivered. The accuracy of positioning the target cell nuclei over the collimator should at least match the spatial resolution of the collimator. Although scattering and beam spreading occur in the collimator edge and the tissue phantom, the dose decreases quickly away from the center of the radiation beam as shown in Figure 4.16. The radiation beam is concentrated on a very small spot area at the entrance plane and spreads out as it travels into the target phantom. It spreads out more quickly if the beam is scattered by the second collimator, demostrated in the right side of Figure 4.16. But the dose at the position sevearal micrometers away from the original radiation beam is one or two orders less than the dose in the center beam.

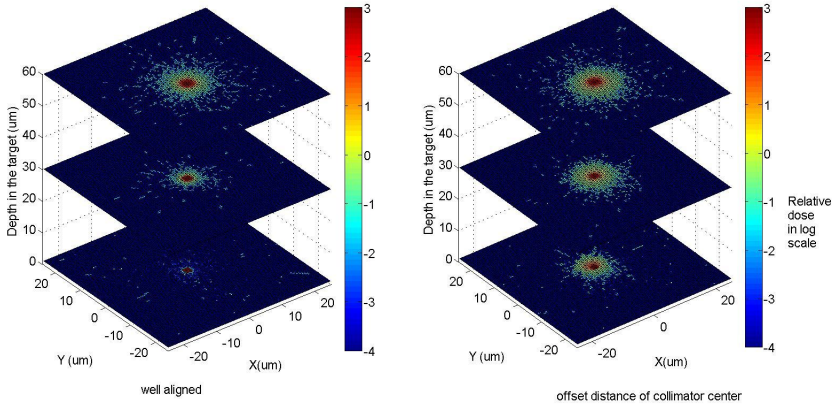

Figure 4.16: Proton beam spreads out quick in the water phatom. 1 million protons were simulated.

The small diameter of the collimated beam and the curveture of the spherical nucleus makes the dose to the nucleus very sensitive to the alignment of the cell nucleus and the collimator. Usually the diameter of a cell nuclus is several micrometers, varying with the size of cells. Figure 4.17 shows dose distribution in the cell nucleus varying with the offset distance of the z-axis of the target nucleus and the collimator. In the simulation setting, the diameter of the target nuclei is 3.3 μm and the radiation beam is created by a 3 μm square steel aperture followed by a 5 μm diameter copper aperture. The blue dashed line shows that the dose still ramain the same if the center of the target nucleus is 1 μm away from the radiation beam center. But if the target nucleus is further away from the beam, radiation dose decreases quickly.

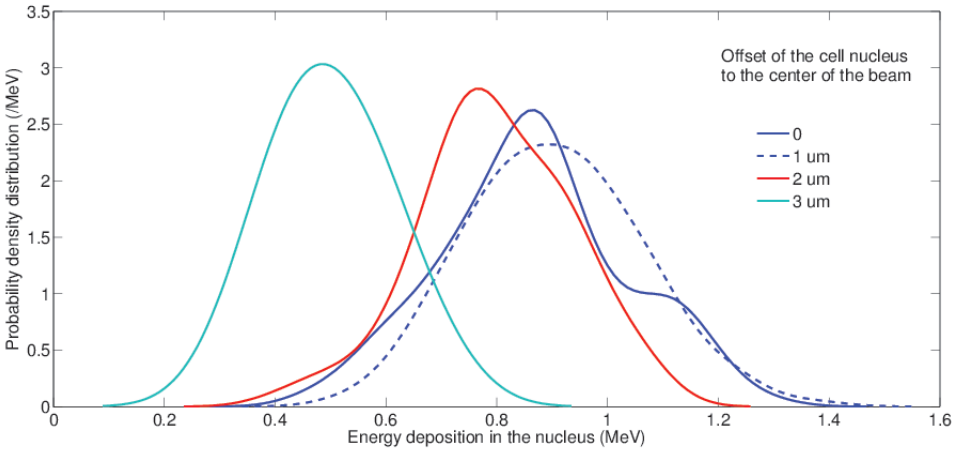

Figure 4.17: Alignment of target nucleus effection on the dose distribution. In the simulation, the target nucleus was located 10 μm depth in the phatom; 1 million 3 MeV protons simulated.

4.2.3 Energy deposition in surrounding cells

The probabilities that surrounding cell nuclei being irradiated were discussed in the beam scattering section. Energy deposition in the non-targeted cells is caused by the large angle scattered primary particles. The range of delta rays is too small to travel to the non-targeted cells if the primary particle remains in the beam. The long distance the primary particle travels in the tissue make the LET of the particle in the non-targeted cell larger than the LET of primary particles in target cell. So energy deposition in the irradiated surrounding cell nucleus is larger than that in the targeted nucleus by one primary particle.

For 2-D cell arrays and 3-D tissues, the probability of surrounding cells to be irradiated is much larger than our simulated results, which is 1 dimension intestine cells.

5. DISCUSSION AND FUTURE PLANS

5.1 Discussion

The simulation results showed that the collimator setup used in the Loma Linda/TAMU experiment can generate a high quality microbeam, with high full energy percentage, and low probability to irradiate a non-targeted cell nucleus.

Scattering from the first aperture is obvious but the large distance between the two apertures makes it very rare for a particle scattered by the first aperture to passing through the second aperture. The scattering from the first aperture should be considered only when the distance between the the apertures is less than 10 mm. The tilt angle between the aperture blade surface and the beam direction, and the rough surface of the blade, are the primary factors that increase the scattering, but the small peaks and valleys on the blade surface contribute more to the scattering.

Scattering from the second aperture is the primary reason for cell nuclei surrounding the target to be irradiated and also causes low energy particles irradiating the target, when the two apertures are not properly aligned or the size of the second aperture is too small. In the Loma Linda/TAMU experiments, the larger diameter of the copper aperture compared to the first aperture allow a certain alignment error, thus improving the system performs and reliability.

Dose to the nucleus is randomly distributed following a normal distribution and depends on the thickness of material the beam has traveled through before reaching it. The lower energy scattered particles from the collimation system could change the energy deposition in the target nucleus. In the experiments when exact number of particles are required to be delivered to the target nucleus, absorbed doses to the target nucleus are more sensitive to the low energy scattered particles. If the

energy of scattered particles is too low to reach the target nucleus, the target nucleus remain unirradiated but the detector still gives the signial that the target nucleus is irradiated as the detector is mounted between the second aperture and the sample holder. If the energy of scattered particles is still large, the dose to the nucleus is larger than normal due to Brag-peak theories.

In the Loma Linda/TAMU experiments, the effects of low energy scattering to the target nucleus could be ignored because about 25 primary particles were delivered to the targeted nucleus, and single particles with lower energy will not significantly affect the dose in the target nucleus. But the large number of primary particles delivered to the target in the experiments increased the probability that surrounding cells would be irradiated.

5.2 Future plans

Although the model of the collimator is an adequate representation of the setup in the experiments, it can be improved to get better results. The basic unit of model of the second aperture uses small tube sections to represent the small ripples in the inner wall of the laser drilled hole in the copper. The morphology of the model is close to the real, but the tinny peaks on the ripples, which may make a significant contribution to the scattering, were not modeled.

The *C. elegans* models were built using Monte Carlo simulation toolkit Geant4. In this models, we constructed different tissues with different atomic compositions to represent the realistic worms and get better data, but there are some limitations. Using Geant4 package, it is difficult to build complex geometries because it uses basic solid structures to form a geometry. Another model which does not rely on Geant 4 is in process. In the new model, all cell nuclei will be included; intestine, skin, neurons, *et al.*

To verify the simulation results, we have to make comparisons with experimental results. The ability to detect the number of particles that traverse the target is a key feature of the microbeam, and also a prerequisite to control the number. A thin detector is usually mounted between the collimator and the target, which reduces the spacial accuracy of the beam. This detector location provides the total number of particles irradiating the target. Another place to site the detector is above the target [18], detecting particles after they traverse the target. This configuration, however, could not be used for situations where the particle only partially penetrates the targets.

The targeting accuracy of the collimator can be evaluated by exposing CR-39 'track-etch' plastic to the particle beam at the sample position then processing using a method introduced by Fews and Henshaw [24, 21, 25]. The passage of a particle is visible on the surface of the plastic as a micron-sized pit. Track detecting plastics are cheap, easy to use, and provide a permanent record of events. Comparing with electronic detectors, which provides energy information only, the plastics shows the geometric distribution of detected particles as well as reflecting the particle energy.

The probabilities of non-targeted cell nuclei to be irradiated can be evaluated using 'track-etch' plastic and other detection methods if the detector could reflect the charged particle position. Using various detection methods, such as surface barrier detectors, the energy deposition in the single nucleus can be measured.

REFERENCES

[1] B. J. Blyth and P. J. Sykes, "Radiation-induced bystander effects: What are they, and how relevant are they to human radiation exposures?," *Radiation Research*, vol. 176, pp. 139–157, 2011.

[2] H. Nagasawa and J. B. Little, "Inudction of sister chromatid exchange by extremely low doses of alpha-particles," *Cancer Research*, vol. 52, pp. 6394–6396, 1992.

[3] V. Anzenberg, S. Chandiramani, and J. A. Coderre, "Let-dependent bystander effects caused by irradiation of human prostate carcinoma cells with x rays or alpha particles," *Radiation Research*, vol. 170, pp. 467–476, 2008.

[4] M. Boyd, A. Sorensen, A. G. McCluskey, and R. J. Mairs, "Radiation quality-dependent bystander effects elicited by targeted radionuclides," *Journal of Pharmacy and Pharmacology*, vol. 60, no. 8, pp. 951–958, 2008.

[5] C. Shao, Y. Furusawa, M. Aoki, H. Matsumoto, and K. Ando, "Nitric oxide-mediated bystander effect induced by heavy-ions in human salivary gland tumour cells," *Internation Journal of Radiation Biology*, vol. 78, no. 9, pp. 837–844, 2002.

[6] E. J. Hall, "The bytander effect," *Health Physics*, vol. 85, no. 1, pp. 31–35, 2003.

[7] S. L. Irons, V. Serra, D. Bowler, K. Chapman, S. M. F. Lyng, and M. Kadhim, "The effects of genetic background and dose on non-targeted effects of radiation," *International Journal of Radiation Biology*, vol. 80, pp. 735–742, Oct 2012.

[8] C. B. Seymour and W. V. Prestwich, "A dose threshold for a medium transfer bystander effect for a human skin cell line," *Radiation Research*, vol. 166, no. 1, pp. 19–23, 2006.

[9] A. M. Hooker, M. Bhat, T. K. Day, J. M. Lane, S. J. Swinburne, A. A. Morleya, and P. J. Sykesa, "The linear no-threshold model does not hold for low-dose ionizing radiation," *Radiation Research*, vol. 162, pp. 447–452, 2004.

[10] M. Tubiana, L. E. Feinendegen, C. Yang, and J. M. Kaminski, "The linear no-threshold relationship is inconsistent with radiation biologic and experimental data," *Radiology*, vol. 251, no. 1, pp. 13–22, 2009.

[11] R. E. Zirkle and W. Bloom, "Irradiation of parts of individual cells," *Science*, vol. 117, pp. 487–493, 1953.

[12] T. K. Hei, L. K. Ballas, david J. Brenner, and C. R. Geard, "Advances in radiobiological studies using a microbeam," *Journal of Radiation Research*, vol. 50, pp. A7–A12, 2009.

[13] S. Gerardi, "A comparative review of charged particle microbeam facilities," *Radiation Protection Dosimetry*, vol. 122, no. 1-4, pp. 285–291, 2006.

[14] M. Folkard, K. M. Prise, G. Grime, K. Kirkby, and B. Vojnovic, "The use of microbeams to investigate radiation damage in living cells," *Applied Radiation and Isotopes*, vol. 67, no. 3, pp. 436–439, 2009.

[15] J. Cookson, "The production and use of a nuclear microprobe of ions at MEV energies," *Nuclear Instruments and Methods*, vol. 165, no. 477–508, 1979.

[16] D. H. Hall and Z. F. Altun, *C. elegans Atlas*. New York: Cold spring harbor laboratory press, 2008.

[17] M. Wolf, F. Nunes, and R. J. Paul, "Coordinates, dna content and heterogeneity of cell nuclei and segments of the caenorhabditis elegans intestine," *Histochemistry and cell biology*, vol. 124, no. 5, pp. 359–367, 2005.

[18] G. Randers-Pehrson, C. R. Geard, G. Johnson, C. D. Elliston, and D. J. Brenner, "The columbia university single-ion microbeam," *Radiation Research*, vol. 156, pp. 210–214, 2001.

[19] A. Weck, T. Crawford, D. Wilkinson, H. Haugen, and J. Preston, "Laser drilling of high aspect ratio holes in copper with femtosecond, picosecond and nanosecond pulses," *Applied Physics A*, vol. 90, no. 3, pp. 537–543, 2008.

[20] F. Long, H. Peng, X. Liu, S. K. Kim, and E. Myers, "A 3d digital atlas of *C. elegans* and its application to single-cell analyses," *Nature Methods*, vol. 6, no. 9, pp. 667–672, 2009.

[21] M. Folkard, B. Vojnovic, K. Hollis, A. Bowey, S. Watts, G. Schettino, K. Prise, and B. Michael, "A charged-particle microbeam: II. a single-particle microcollimation and detection system.," *International Journal of Radiation Biology*, vol. 72, no. 4, pp. 387–395, 1997.

[22] F. H. Attix, *Introduction to Radiological Physics and Radiation Dosimetry*. Weinheim, Germany: Wiley-VCH, 2004.

[23] I. C. on Radiation Units and Measurements, *Stopping Powers and Ranges for Protons and Alpha Particles*. Bethesda, Maryland: ICRU, 1993.

[24] A. Fews and D. Henshaw, "High resolution alpha particle spectroscopy using cr-39 plastic track detector," *Nuclear Instruments and Methods in Physics Research*, vol. 197, no. 2, pp. 517–529, 1982.

[25] O. Bondarenko, P. Salmon, D. Henshaw, and A. Fews, "Performance of alpha particle spectroscopy using a tastrak detector," *Radiation Measurements*, vol. 26, no. 1, pp. 59–64, 1996.

APPENDIX A

PARAMETERS USED IN GEANT4 CODES

Table A.1: Randomly generated height of the peaks on the surface of 4 steel blades (μm)

0.1746	0.5586	0.1270	0.6258	0.1188	0.5104	0.0852	0.3881	0.4009	0.2517
0.2343	0.1107	0.0295	0.5266	0.0403	0.1362	0.4295	0.4971	0.1156	0.1280
0.1088	0.0443	0.2426	0.3662	0.3211	0.1424	0.0715	0.4055	0.5076	0.0207
0.0208	0.4583	0.0526	0.1976	0.2362	0.2336	0.0785	0.2068	0.3388	0.2317
0.1246	0.4145	0.2065	0.0707	0.1374	0.7994	0.3659	0.2093	0.6996	0.2777
0.1748	0.2029	0.6011	0.3643	0.1055	0.1936	0.0629	0.4347	0.0747	0.5667
0.1576	0.1376	0.3129	0.2012	0.1077	0.2333	0.4468	0.2709	0.6285	0.3158
0.5829	0.1433	0.1665	0.4130	0.0510	0.0189	0.0610	0.0216	0.0382	0.0934
0.0236	0.2676	0.3622	0.2727	0.0721	0.6459	0.1647	0.0385	0.4394	0.2601
0.1023	0.0227	0.1541	0.0800	0.0024	0.2744	0.6202	0.3567	0.0623	0.0095
0.2027	0.1819	0.2839	0.3025	0.4931	0.2153	0.1126	0.5247	0.2885	0.5481
0.3778	0.1873	0.0495	0.4725	0.3464	0.3781	0.1759	0.4402	0.5567	0.6768
0.1701	0.2387	0.3170	0.2327	0.1952	0.3591	0.3329	0.7319	0.1765	0.6250
0.1375	0.1050	0.1125	0.1782	0.3973	0.1209	0.0551	0.1004	0.1322	0.1665
0.0648	0.1628	0.1511	0.6226	0.7657	0.0017	0.2300	0.8578	0.5752	0.4431
0.2199	0.2421	0.0929	0.2463	0.3112	0.4311	0.6376	0.2825	0.5766	0.3120
0.2226	0.4494	0.1138	0.1211	0.2149	0.0624	0.1671	0.2206	0.0950	0.2283
0.1555	0.0510	0.1615	0.0164	0.3571	0.1831	0.3739	0.3025	0.1051	0.3013
0.2008	0.0185	0.0643	0.4501	0.2510	0.1784	0.3751	0.1172	0.4782	0.6663

The laser hole in the 25.4 μm thickness copper is tapered. Geant4 Solid geometry class G4Cons was used to built the laser hole and ripples on the inner wall. G4Cons is defined by the following parameters (Geant4 toolkit could be downloaded from http://geant4.cern.ch/):

pRmin1	inside radius at -pDz
pRmax1	outside radius at -pDz
pRmin2	inside radius at +pDz
pRmax2	outside radius at +pDz
pDz	half length in z
pSPhi	starting angle of the segment in radians
pDPhi	the angle of the segment in radians

Table A.2: Parameters of the 5 μm diameter laser hole

pRmin1 (μm)	0
pRmax1 (μm)	2.5
pRmin2 (μm)	0
pRmax2 (μm)	2.8
pDz (μm)	12.7
pSPhi (degree)	0
pDPhi (degree)	360

Table A.3: Parameters for different diameters of lasor holes (μm)

Diameter	0.3	0.6	0.8	1.4
PRmax1	0.15	0.3	0.4	0.7
pRmax2	0.2	0.5	0.6	0.9
Ripple H mean	0.04	0.08	0.09	0.14
Ripple H STD	0.01	0.015	0.02	0.02

Ripple H mean: mean height of the ripples.
Ripple H STD: standerd deviation of the heights.

The ripples were randomly generated. The thickness, which equals to pRmax-pRmin, follows Gaussian distribution with an average of 0.14 μm, standard deviation of 0.02 μm, minimum of 0, and maximum is 0.2 μm. The length of a section unit is 0.5 μm. Table A.4 listed parts of the sections randomly generated when simulating.

Table A.4: Randomly generated small ripples on the inner surface of the laser hole (μm)

Z	pSPhi	spanPhi	Thickness	pRmin1	pRmax1	pRmin2	pRmax2
-12.45	0	9.62506	0.131573	2.66843	2.8	2.6763	2.80787
-12.45	12.2236	7.45436	0.119099	2.6809	2.8	2.68877	2.80787
-12.45	23.0024	9.65544	0.137658	2.66234	2.8	2.67022	2.80787
-12.45	36.0094	6.37428	0.152176	2.64782	2.8	2.6557	2.80787
-12.45	45.2713	5.90315	0.153408	2.64659	2.8	2.65447	2.80787
-12.45	53.5922	5.96642	0.141519	2.65848	2.8	2.66636	2.80787
-12.45	62.7587	9.92221	0.143111	2.65689	2.8	2.66476	2.80787
-12.45	76.0178	6.92478	0.135051	2.66495	2.8	2.67282	2.80787
-12.45	85.9567	6.61292	0.133757	2.66624	2.8	2.67412	2.80787
-12.45	94.9649	5.58403	0.117099	2.6829	2.8	2.69077	2.80787

continued on next page

–continued from previous page

Z	pSPhi	spanPhi	Thickness	pRmin1	pRmax1	pRmin2	pRmax2
-12.45	104.008	6.58371	0.137091	2.66291	2.8	2.67078	2.80787
-12.45	113.541	7.00609	0.149511	2.65049	2.8	2.65836	2.80787
-12.45	123.546	8.88436	0.141777	2.65822	2.8	2.6661	2.80787
-12.45	135.52	7.98424	0.136336	2.66366	2.8	2.67154	2.80787
-12.45	146.552	7.97175	0.16257	2.63743	2.8	2.6453	2.80787
-12.45	157.059	5.95608	0.124592	2.67541	2.8	2.68328	2.80787
-12.45	165.591	6.53229	0.129463	2.67054	2.8	2.67841	2.80787
-12.45	175.069	5.8603	0.162039	2.63796	2.8	2.64583	2.80787
-12.45	183.899	7.93884	0.148504	2.6515	2.8	2.65937	2.80787
-12.45	194.855	7.81488	0.160441	2.63956	2.8	2.64743	2.80787
-12.45	205.703	7.12878	0.140602	2.6594	2.8	2.66727	2.80787
-12.45	215.996	7.56616	0.19361	2.60639	2.8	2.61426	2.80787
-12.45	226.597	6.53884	0.155201	2.6448	2.8	2.65267	2.80787
-12.45	236.39	7.53965	0.128446	2.67155	2.8	2.67943	2.80787
-12.45	247.259	6.24594	0.151023	2.64898	2.8	2.65685	2.80787
-12.45	256.412	6.73965	0.126856	2.67314	2.8	2.68102	2.80787
-12.45	266.859	7.30441	0.133289	2.66671	2.8	2.67459	2.80787
-12.45	277.298	7.20131	0.138962	2.66104	2.8	2.66891	2.80787
-12.45	287.469	7.33725	0.129763	2.67024	2.8	2.67811	2.80787
-12.45	297.651	7.59448	0.135361	2.66464	2.8	2.67251	2.80787
-12.45	308.438	7.78711	0.146439	2.65356	2.8	2.66144	2.80787
-12.45	318.847	7.12267	0.134438	2.66556	2.8	2.67344	2.80787

continued on next page

–continued from previous page

Z	pSPhi	spanPhi	Thickness	pRmin1	pRmax1	pRmin2	pRmax2
-12.45	328.86	7.13877	0.123325	2.67667	2.8	2.68455	2.80787
-12.45	338.918	6.51394	0.159402	2.6406	2.8	2.64847	2.80787
-12.45	348.632	7.27693	0.120326	2.67967	2.8	2.68755	2.80787
-11.95	0	7.78919	0.151753	2.65612	2.80787	2.66399	2.81575
-11.95	10.2784	6.49431	0.111516	2.69636	2.80787	2.70423	2.81575
-11.95	19.7632	7.24173	0.165844	2.64203	2.80787	2.6499	2.81575
-11.95	29.7111	7.38053	0.148916	2.65896	2.80787	2.66683	2.81575
-11.95	40.0472	7.06327	0.0980821	2.70979	2.80787	2.71767	2.81575
-11.95	49.6668	6.59143	0.112108	2.69577	2.80787	2.70364	2.81575
-11.95	59.2488	7.16568	0.16316	2.64471	2.80787	2.65259	2.81575
-11.95	69.7448	6.94699	0.129995	2.67788	2.80787	2.68575	2.81575
-11.95	79.6158	8.62298	0.147857	2.66002	2.80787	2.66789	2.81575
-11.95	91.2061	7.25653	0.135638	2.67224	2.80787	2.68011	2.81575
-11.95	101.274	7.05305	0.122601	2.68527	2.80787	2.69315	2.81575
-11.95	111.695	7.97304	0.120288	2.68759	2.80787	2.69546	2.81575
-11.95	122.894	6.94124	0.148332	2.65954	2.80787	2.66742	2.81575
-11.95	132.887	6.66306	0.142306	2.66557	2.80787	2.67344	2.81575
-11.95	142.299	9.74225	0.141827	2.66605	2.80787	2.67392	2.81575
-11.95	155.003	8.58089	0.144969	2.66291	2.80787	2.67078	2.81575
-11.95	166.489	6.54884	0.149891	2.65798	2.80787	2.66586	2.81575
-11.95	176.271	6.37549	0.135947	2.67193	2.80787	2.6798	2.81575
-11.95	185.359	7.07206	0.131763	2.67611	2.80787	2.68398	2.81575

continued on next page

–continued from previous page

Z	pSPhi	spanPhi	Thickness	pRmin1	pRmax1	pRmin2	pRmax2
-11.95	195.518	6.68501	0.134424	2.67345	2.80787	2.68132	2.81575
-11.95	204.785	7.576	0.161096	2.64678	2.80787	2.65465	2.81575
-11.95	215.335	5.99098	0.1128	2.69507	2.80787	2.70295	2.81575
-11.95	223.812	6.96638	0.161917	2.64596	2.80787	2.65383	2.81575
-11.95	233.839	7.4737	0.140743	2.66713	2.80787	2.67501	2.81575
-11.95	244.641	8.25666	0.13772	2.67015	2.80787	2.67803	2.81575
-11.95	256.118	9.07287	0.128532	2.67934	2.80787	2.68722	2.81575
-11.95	268.66	5.84159	0.142362	2.66551	2.80787	2.67339	2.81575
-11.95	277.648	7.92628	0.171811	2.63606	2.80787	2.64394	2.81575
-11.95	288.39	6.24319	0.141298	2.66658	2.80787	2.67445	2.81575
-11.95	297.193	6.38372	0.139794	2.66808	2.80787	2.67595	2.81575
-11.95	307.087	8.05039	0.146288	2.66159	2.80787	2.66946	2.81575
-11.95	318.203	6.7296	0.130465	2.67741	2.80787	2.68528	2.81575
-11.95	328.526	7.45761	0.162729	2.64514	2.80787	2.65302	2.81575
-11.95	339.983	6.23988	0.141475	2.6664	2.80787	2.67427	2.81575

Table A.5: L1 stage worm body dimensions (μm)

Name	Size (μm)
Body dimeter	20
Skin thickness	1.0
Cuticle depth	0.1
Intestine length	125
Muscle depth	0.4
Nucleus radius	3.3

Table A.6: Intestine cell nuclei positions

Intestine	Ventral (μm)			Dorsal (μm)		
	AP	DV	LR	AP	DV	LR
2	9.4	5	0	9.4	-5	0
3	21.5	5	0	19.5	-5	0
4	35.4	4.92	0.87	31.4	-4.92	-0.87
5	48.9	0	5	43.1	0	-5
6	57.5	-0.87	4.92	64.2	0.87	-4.92
7	72.4	-1.71	4.7	77.9	1.71	-4.7
8	87.2	-2.5	4.33	91.1	2.5	-4.33
9	97.5	-5	0	99.9	5	0

AP: center locations of each cell nucleus along the anterior-posterior axes relative to intestine 1.
DV: center locations of each cell nucleus along dorsal-ventral axes.
DV: center locations of each cell nucleus along left-right axes.

APPENDIX B

ENERGY DEPOSITION DATA

Table B.1 shows the energy deposition to a single cell nucleus by simulating around 5000 protons to get 1000 protons hitting a cell nucleus. In the simulation, the targeted cell nucleus is 6D, and the offset of the two apertures were is 2 μm. The particle # in the table shows order of the protons in the simulation, and the accumulated # shows the total number of particles that hitted the worm body from the beginning of the simulation.

Table B.1: Energy deposition to nucleus by 3 MeV protons

Index	Partical #	Accumulated #(hitting the worm)	Nucleus	Edep(MeV)
1	2	1	6D	0.038408019
2	13	4	6D	0.005799484
3	14	5	6D	0.026701755
4	33	12	6D	0.026535572
5	34	13	6D	0.056664333
6	39	15	6D	0.05500851
7	42	16	6D	0.03867993
8	46	18	6D	0.044251283
9	48	19	6D	0.044983288
10	51	22	6D	0.000753689
11	54	23	6D	0.041610105
12	55	24	6D	0.040667062

continued on next page

–continued from previous page

Index	Partical #	Accumulated #(hitting the worm)	Nucleus	Edep(MeV)
13	57	25	6D	0.038882265
14	65	28	6D	0.035971069
15	66	29	6D	0.01399115
16	73	32	6D	0.039465574
17	80	34	6D	0.037044793
18	81	35	6D	0.053178078
19	84	37	6D	0.037508366
20	87	40	6D	0.024721944
21	89	41	6D	0.001343226
22	93	43	6D	0.025810437
23	95	44	6D	0.030047435
24	96	45	6D	0.002856877
25	98	47	6D	0.025032637
26	99	48	6D	0.008952064
27	105	51	6D	0.019269116
28	106	52	6D	0.012740437
29	116	55	6D	0.054657816
30	117	56	6D	0.031493302
31	120	57	6D	0.062938487
32	124	58	6D	0.041908079
33	127	60	6D	0.020969985
34	137	61	6D	0.028948578

continued on next page

–continued from previous page

Index	Partical #	Accumulated #(hitting the worm)	Nucleus	Edep(MeV)
35	153	64	6D	0.02896023
36	155	66	6D	0.034676455
37	160	71	6D	0.032764002
38	174	75	6D	0.027578705
39	177	77	6D	0.044433122
40	181	78	6D	0.043776766
41	190	84	6D	0.013139315
42	193	85	6D	0.0652474
43	201	89	6D	0.048540913
44	202	90	6D	0.084130198
45	211	93	6D	0.037906941
46	213	94	6D	0.016703744
47	220	97	6D	0.048183243
48	226	100	6D	0.035003323
49	235	103	6D	0.040482604
50	241	105	6D	0.031548648
51	252	107	6D	0.015191215
52	256	109	6D	0.037974292
53	257	110	6D	0.148081938
54	260	111	6D	0.041493281
55	264	113	6D	0.031810686
56	270	114	6D	0.050384495

continued on next page

–continued from previous page

Index	Partical #	Accumulated #(hitting the worm)	Nucleus	Edep(MeV)
57	271	115	6D	0.019641645
58	272	116	6D	0.046884226
59	282	119	6D	0.039816897
60	283	120	6D	0.033534972
61	289	124	6D	0.037817023
62	293	125	6D	0.04059366
63	295	126	6D	0.039696409
64	296	127	6D	0.034993636
65	304	130	6D	0.026781277
66	305	131	6D	0.026679295
67	309	133	6D	0.019310977
68	311	134	6D	0.03622104
69	323	137	6D	0.039676877
70	324	138	6D	0.043219973
71	326	139	6D	0.04715757
72	328	140	6D	0.041161056
73	329	141	6D	0.015984744
74	330	142	6D	0.048659896
75	336	144	6D	0.032962851
76	338	146	6D	0.049821251
77	340	147	6D	0.01205089
78	341	148	6D	0.066722731

continued on next page

–continued from previous page

Index	Partical #	Accumulated #(hitting the worm)	Nucleus	Edep(MeV)
79	350	154	6D	0.023998409
80	355	156	6D	0.037986883
81	356	157	6D	0.023845054
82	359	159	6D	0.024437942
83	367	161	6D	0.000589785
84	371	163	6D	0.03409022
85	373	164	6D	0.037102668
86	374	165	6D	0.033911184
87	387	171	6D	0.059372208
88	391	174	6D	0.019668333
89	395	177	6D	0.059282819
90	396	178	6D	0.016792924
91	400	181	6D	0.035783548
92	401	182	6D	0.033617222
93	407	184	6D	0.040562476
94	410	186	6D	0.034902669
95	411	187	6D	0.036682665
96	413	188	6D	0.026792627
97	415	189	6D	0.044470003
98	420	190	6D	0.038718579
99	421	191	6D	0.029366308
100	422	192	6D	0.026292299

continued on next page

–continued from previous page

Index	Partical #	Accumulated #(hitting the worm)	Nucleus	Edep(MeV)
101	424	193	6D	0.033296081
102	429	194	6D	0.027829759
103	437	199	6D	0.035370559
104	456	202	6D	0.033542458
105	459	203	6D	0.046357515
106	460	204	6D	0.039458677
107	468	208	6D	0.02386937
108	472	209	6D	0.029184324
109	484	213	6D	0.05399002
110	486	214	6D	0.059401045
111	493	217	6D	0.020110664
112	498	220	6D	0.039616782
113	506	221	6D	0.035097955
114	519	224	6D	0.039794345
115	520	225	6D	0.035449522
116	521	226	6D	0.034586211
117	523	228	6D	0.031150067
118	526	230	6D	0.034154491
119	537	235	6D	0.047098479
120	542	238	6D	0.038243264
121	546	239	6D	0.038289252
122	554	242	6D	0.00413841

continued on next page

–continued from previous page

Index	Partical #	Accumulated #(hitting the worm)	Nucleus	Edep(MeV)
123	556	243	6D	0.036057573
124	566	244	6D	0.049297305
125	579	249	6D	0.042138047
126	583	250	6D	0.029559378
127	592	252	6D	0.045068176
128	595	254	6D	0.02402895
129	596	255	6D	0.087709483
130	597	256	6D	0.038019776
131	598	257	6D	0.024203796
132	604	260	6D	0.020529451
133	607	261	6D	0.01583108
134	617	263	6D	0.095880845
135	619	264	6D	0.030073511
136	622	265	6D	0.076057793
137	625	267	6D	0.014780659
138	626	268	6D	0.050191094
139	628	269	6D	0.023581063
140	630	270	6D	0.035247831
141	636	274	6D	0.041476924
142	641	277	6D	0.031007465
143	645	278	6D	0.036840197
144	647	279	6D	0.032952307

continued on next page

–continued from previous page

Index	Partical #	Accumulated #(hitting the worm)	Nucleus	Edep(MeV)
145	656	282	6D	0.02566536
146	674	290	6D	0.028824478
147	683	293	6D	0.021832371
148	684	294	6D	0.086958264
149	686	295	6D	0.043825614
150	702	298	6D	0.021172434
151	707	300	6D	0.022654988
152	709	301	6D	0.036119411
153	710	302	6D	0.056924006
154	715	306	6D	0.043389074
155	716	307	6D	0.083327099
156	723	311	6D	0.024693067
157	724	312	6D	0.036600354
158	726	313	6D	0.018001267
159	727	314	6D	0.112966566
160	728	315	6D	0.018411422
161	730	316	6D	0.02875997
162	736	319	6D	0.044139264
163	740	321	6D	0.037836977
164	745	323	6D	0.01578675
165	750	324	6D	0.023978376
166	754	325	6D	0.043940497

continued on next page

–continued from previous page

Index	Partical #	Accumulated #(hitting the worm)	Nucleus	Edep(MeV)
167	755	326	6D	0.028953036
168	758	327	6D	0.038641396
169	771	330	6D	0.024409755
170	779	333	6D	0.035967174
171	781	335	6D	0.005705782
172	785	336	6D	0.04488122
173	794	338	6D	0.013351438
174	805	340	6D	0.069928374
175	807	341	6D	0.036435328
176	809	342	6D	0.02934748
177	815	345	6D	0.029016697
178	818	346	6D	0.034096383
179	821	348	6D	0.026804627
180	822	349	6D	0.03600799
181	824	350	6D	0.033920494
182	827	351	6D	0.019264268
183	830	352	6D	0.034148926
184	833	353	6D	0.016658112
185	846	357	6D	0.030477685
186	847	358	6D	0.02675274
187	855	363	6D	0.046001516
188	869	370	6D	0.034916385

continued on next page

–continued from previous page

Index	Partical #	Accumulated #(hitting the worm)	Nucleus	Edep(MeV)
189	873	373	6D	0.010772797
190	874	374	6D	0.031485188
191	881	376	6D	0.005735168
192	882	377	6D	0.021962033
193	884	379	6D	0.056512041
194	886	380	6D	0.082610508
195	892	382	6D	0.009983613
196	893	383	6D	0.046423316
197	894	384	6D	0.019669947
198	895	385	6D	0.069941071
199	897	387	6D	0.017042899
200	900	388	6D	0.024752278
201	910	391	6D	0.045303267
202	916	392	6D	0.021581519
203	919	394	6D	0.051622382
204	924	397	6D	0.012402997
205	928	399	6D	0.027958484
206	932	400	6D	0.042185718
207	939	402	6D	0.002517146
208	947	404	6D	0.029732426
209	953	406	6D	0.041582089
210	958	408	6D	0.035135837

continued on next page

–continued from previous page

Index	Partical #	Accumulated #(hitting the worm)	Nucleus	Edep(MeV)
211	960	409	6D	0.037146334
212	961	410	6D	0.043275498
213	962	411	6D	0.00829891
214	977	415	6D	0.044156947
215	981	418	6D	0.050429949
216	988	421	6D	0.012826327
217	989	422	6D	0.031337646
218	990	423	6D	0.006930222
219	991	424	6D	0.014014714
220	994	426	6D	0.011116486
221	1003	428	6D	0.022794075
222	1012	432	6D	0.00908325
223	1014	433	6D	0.021275225
224	1016	434	6D	0.078857432
225	1019	436	6D	0.03858419
226	1029	440	6D	0.043711861
227	1041	445	6D	0.04452962
228	1045	447	6D	0.04188299
229	1046	448	6D	0.060247659
230	1053	450	6D	0.013065383
231	1054	451	6D	0.08755051
232	1056	452	6D	0.026752936

continued on next page

–continued from previous page

Index	Partical #	Accumulated #(hitting the worm)	Nucleus	Edep(MeV)
233	1058	453	6D	0.03033791
234	1068	455	6D	0.040207608
235	1072	457	7D	0.07090113
236	1076	459	6D	0.021552935
237	1077	460	6D	0.016562235
238	1079	461	6D	0.047431833
239	1082	463	6D	0.021633117
240	1083	464	6D	0.016788691
241	1088	468	6D	0.001340419
242	1090	469	6D	0.039884385
243	1098	474	6D	0.030256986
244	1099	475	6D	0.009726013
245	1101	477	6D	0.028323544
246	1102	478	6D	0.027259798
247	1103	479	6D	0.000834364
248	1104	480	6D	0.037522165
249	1105	481	6D	0.066026399
250	1106	482	6D	0.039527443
251	1116	486	6D	0.034159541
252	1117	487	6D	0.001671994
253	1119	488	6D	0.018145789
254	1128	493	6D	0.0332798

continued on next page

–continued from previous page

Index	Partical #	Accumulated #(hitting the worm)	Nucleus	Edep(MeV)
255	1132	494	6D	0.023294559
256	1139	496	6D	0.021637078
257	1142	497	6D	0.024975603
258	1146	499	6D	0.081594304
259	1150	501	6D	0.045256674
260	1156	502	6D	0.036413199
261	1161	504	6D	0.011644161
262	1163	505	6D	0.027383447
263	1164	506	6D	0.008872172
264	1165	507	6D	0.021797917
265	1166	508	6D	0.089100209
266	1179	510	6D	0.04102238
267	1181	511	6D	0.052370048
268	1184	513	6D	0.010891679
269	1185	514	6D	0.028784142
270	1190	515	6D	0.037507787
271	1199	517	6D	0.047276409
272	1202	518	6D	0.036507992
273	1203	519	6D	0.031701916
274	1209	521	6D	0.046388786
275	1211	522	6D	0.02077202
276	1214	524	6D	0.031519559

continued on next page

–continued from previous page

Index	Partical #	Accumulated #(hitting the worm)	Nucleus	Edep(MeV)
277	1215	525	6D	0.02783245
278	1219	527	6D	0.04903871
279	1220	528	6D	0.03376849
280	1222	529	6D	0.006372026
281	1225	531	6D	0.076323563
282	1230	532	6D	0.047293203
283	1235	535	6D	0.022992306
284	1243	539	6D	0.000841649
285	1250	541	6D	0.032558015
286	1256	542	6D	0.021571475
287	1257	543	6D	0.03229711
288	1258	544	6D	0.076065512
289	1262	545	6D	0.043754249
290	1263	546	6D	0.03155722
291	1265	547	6D	0.027740329
292	1274	548	6D	0.043031499
293	1279	551	6D	0.016544848
294	1282	553	6D	0.061525433
295	1287	554	6D	0.057614776
296	1290	556	6D	0.027915
297	1298	559	6D	0.041014204
298	1300	560	6D	0.037756652

continued on next page

–continued from previous page

Index	Partical #	Accumulated #(hitting the worm)	Nucleus	Edep(MeV)
299	1303	562	6D	0.045528933
300	1309	563	6D	0.025509648
301	1316	564	6D	0.047162067
302	1318	565	6D	0.008631742
303	1321	566	6D	0.032397711
304	1326	568	6D	0.037053837
305	1327	569	6D	0.016194945
306	1331	571	6D	0.01340233
307	1338	575	6D	0.014903196
308	1344	577	6D	0.0269831
309	1348	579	6D	0.010246248
310	1354	582	6D	0.016297845
311	1358	584	6D	0.025082579
312	1359	585	6D	0.03098259
313	1369	587	6D	0.023210539
314	1374	589	6D	0.002215694
315	1383	593	6D	0.014759405
316	1384	594	6D	0.022786325
317	1386	595	6D	0.003604641
318	1389	596	6D	0.001078584
319	1393	598	6D	0.029825195
320	1397	602	6D	0.047946393

continued on next page

–continued from previous page

Index	Partical #	Accumulated #(hitting the worm)	Nucleus	Edep(MeV)
321	1398	603	6D	0.050619532
322	1405	606	6D	0.038118649
323	1409	608	6D	0.049471913
324	1410	609	6D	0.028049669
325	1412	610	6D	0.045528284
326	1424	615	6D	0.043017368
327	1427	616	6D	0.057228066
328	1429	617	6D	0.023049529
329	1438	621	6D	0.039516869
330	1439	622	6D	0.038412144
331	1441	623	6D	0.030573958
332	1452	625	6D	0.061886914
333	1457	626	6D	0.016327707
334	1466	629	6D	0.033986804
335	1469	630	6D	0.019997631
336	1471	631	6D	0.042043793
337	1476	632	6D	0.046944723
338	1479	634	6D	0.018903512
339	1483	635	6D	0.047487808
340	1484	636	6D	0.018131145
341	1490	640	6D	0.022301018
342	1491	641	6D	0.028078034

continued on next page

–continued from previous page

Index	Partical #	Accumulated #(hitting the worm)	Nucleus	Edep(MeV)
343	1500	644	6D	0.03278163
344	1508	648	6D	0.034820644
345	1509	649	6D	0.018863347
346	1511	650	6D	0.046450144
347	1514	651	6D	0.030389657
348	1515	652	6D	0.016401281
349	1520	655	6D	0.032522054
350	1523	657	6D	0.002787039
351	1538	663	6D	0.028391252
352	1539	664	6D	0.023522995
353	1544	667	6D	0.039863611
354	1553	673	6D	0.041533931
355	1559	677	6D	0.039761556
356	1560	678	6D	0.049580547
357	1564	680	6D	0.03495959
358	1571	682	6D	0.037760488
359	1572	683	6D	0.043748952
360	1573	684	6D	0.086125671
361	1581	688	6D	0.028513644
362	1583	689	6D	0.049586052
363	1590	692	6D	0.019096993
364	1598	695	6D	0.028083715

continued on next page

–continued from previous page

Index	Partical #	Accumulated #(hitting the worm)	Nucleus	Edep(MeV)
365	1614	698	6D	0.022641463
366	1620	700	6D	0.022584552
367	1624	702	6D	0.037771681
368	1627	704	6D	0.026578862
369	1628	705	6D	0.011591881
370	1629	706	6D	0.057673164
371	1632	708	6D	0.035053279
372	1633	709	6D	0.045476858
373	1634	710	6D	0.065168533
374	1638	712	6D	0.096431317
375	1639	713	6D	0.04875577
376	1643	715	6D	0.030203134
377	1644	716	6D	0.043052876
378	1645	717	6D	0.017105915
379	1649	718	6D	0.040278311
380	1652	720	6D	0.007319819
381	1653	721	6D	0.043455887
382	1663	725	6D	0.037005687
383	1667	727	6D	0.042282612
384	1673	729	6D	0.042090455
385	1681	731	6D	0.026654085
386	1691	738	6D	0.031495014

continued on next page

–continued from previous page

Index	Partical #	Accumulated #(hitting the worm)	Nucleus	Edep(MeV)
387	1700	742	6D	0.04363964
388	1706	744	6D	0.006620722
389	1708	746	6D	0.029595623
390	1711	748	6D	0.025874433
391	1722	752	6D	0.023962472
392	1725	753	6D	0.001599429
393	1727	754	6D	0.031792988
394	1733	757	6D	0.038685584
395	1736	759	6D	0.039995033
396	1737	760	6D	0.033534564
397	1745	764	6D	0.047904414
398	1756	770	6D	0.022490652
399	1760	772	6D	0.026401933
400	1762	774	6D	0.025670226
401	1765	775	6D	0.043107085
402	1768	776	6D	0.054293156
403	1774	779	6D	0.061294566
404	1777	781	6D	0.043511957
405	1778	782	6D	0.012097695
406	1783	783	6D	0.042779011
407	1789	787	6D	0.073577696
408	1799	790	6D	0.042173046

continued on next page

–continued from previous page

Index	Partical #	Accumulated #(hitting the worm)	Nucleus	Edep(MeV)
409	1801	791	6D	0.037329715
410	1803	793	6D	0.04132443
411	1805	794	6D	0.032673165
412	1806	795	6D	0.009275185
413	1807	796	6D	0.044915744
414	1808	797	6D	0.035288945
415	1811	799	6D	0.0097021
416	1821	804	6D	0.027299187
417	1824	807	6D	0.047451762
418	1836	812	6D	0.031281142
419	1837	813	6D	0.025560633
420	1838	814	6D	0.044606928
421	1854	818	6D	0.040495983
422	1859	820	6D	0.057208585
423	1866	823	6D	0.047088053
424	1870	824	6D	0.052674252
425	1871	825	6D	0.037286291
426	1872	826	6D	0.014590471
427	1873	827	6D	0.041618679
428	1877	829	6D	0.04024779
429	1883	831	6D	0.033900343
430	1891	836	6D	0.013784305

continued on next page

–continued from previous page

Index	Partical #	Accumulated #(hitting the worm)	Nucleus	Edep(MeV)
431	1896	837	6D	0.026538661
432	1898	838	6D	0.027075677
433	1901	840	6D	0.025473601
434	1905	841	6D	0.023230788
435	1909	842	6D	0.044236819
436	1914	843	6D	0.033296092
437	1915	844	6D	0.043538869
438	1920	845	6D	0.040658668
439	1921	846	6D	0.003075945
440	1922	847	6D	0.013805151
441	1923	848	6D	0.046424495
442	1928	850	6D	0.031195862
443	1932	853	6D	0.041672843
444	1933	854	6D	0.038980036
445	1943	856	6D	0.018976496
446	1951	859	6D	0.019734609
447	1964	866	6D	0.012101809
448	1970	869	6D	0.03107981
449	1975	871	6D	0.024547998
450	1978	872	6D	0.028766626
451	1999	880	6D	0.046774344
452	2001	881	6D	0.029011446

continued on next page

–continued from previous page

Index	Partical #	Accumulated #(hitting the worm)	Nucleus	Edep(MeV)
453	2005	884	6D	0.035214969
454	2006	885	6D	0.005026442
455	2007	886	6D	0.002149288
456	2008	887	6D	0.019984363
457	2021	894	6D	0.036030501
458	2025	895	6D	0.029960592
459	2034	898	6D	0.037324296
460	2035	899	6D	0.02015228
461	2039	901	6D	0.028588962
462	2047	906	6D	0.023631272
463	2051	909	6D	0.027044524
464	2053	910	6D	0.037284342
465	2054	911	6D	0.021026881
466	2066	918	6D	0.019384157
467	2072	920	6D	0.039134343
468	2073	921	6D	0.023324828
469	2080	923	6D	0.033282315
470	2083	924	6D	0.013390577
471	2086	925	6D	0.024365827
472	2087	926	6D	0.045419259
473	2088	927	6D	0.030699882
474	2100	933	6D	0.033431173

continued on next page

–continued from previous page

Index	Partical #	Accumulated #(hitting the worm)	Nucleus	Edep(MeV)
475	2102	934	6D	0.038771202
476	2110	938	6D	0.008952831
477	2114	941	6D	0.05288481
478	2115	942	6D	0.043100016
479	2117	943	6D	0.048261341
480	2119	944	6D	0.007861959
481	2131	952	6D	0.022191805
482	2136	954	6D	0.041114121
483	2137	955	6D	0.036458869
484	2144	958	6D	0.042573861
485	2156	963	6D	0.046361609
486	2163	967	6D	0.022704858
487	2169	969	6D	0.045958519
488	2172	971	6D	0.190879268
489	2177	972	6D	0.010913828
490	2198	977	6D	0.036251213
491	2200	978	6D	0.043405432
492	2201	979	6D	0.028504708
493	2203	980	6D	0.014579393
494	2209	981	6D	0.030758844
495	2226	986	6D	0.032103597
496	2228	987	6D	0.020580983

continued on next page

–continued from previous page

Index	Partical #	Accumulated #(hitting the worm)	Nucleus	Edep(MeV)
497	2239	990	6D	0.006217268
498	2252	997	6D	0.053468246
499	2254	998	6D	0.005957864
500	2263	1003	6D	0.019443995
501	2264	1004	6D	0.03571441
502	2266	1005	6D	0.041341889
503	2271	1008	6D	0.06793181
504	2277	1010	6D	0.021810959
505	2278	1011	6D	0.021183633
506	2280	1013	6D	0.031745425
507	2295	1017	6D	0.032705066
508	2300	1019	6D	0.035000083
509	2301	1020	6D	0.021567132
510	2315	1027	6D	0.018381497
511	2317	1029	6D	0.016839356
512	2318	1030	6D	0.105250691
513	2322	1031	6D	0.014211223
514	2329	1035	6D	0.048126341
515	2343	1040	6D	0.017032826
516	2346	1041	6D	0.041316705
517	2348	1043	6D	0.040888048
518	2350	1045	6D	0.022696008

continued on next page

–continued from previous page

Index	Partical #	Accumulated #(hitting the worm)	Nucleus	Edep(MeV)
519	2352	1047	6D	0.044829719
520	2354	1048	6D	0.022782978
521	2362	1051	6D	0.077395931
522	2367	1054	6D	0.022248289
523	2369	1055	6D	0.045588118
524	2370	1056	6D	0.031631676
525	2373	1058	6D	0.032642787
526	2374	1059	6D	0.059736242
527	2385	1063	6D	0.027713026
528	2388	1064	6D	0.029893191
529	2393	1066	6D	0.035320897
530	2395	1067	6D	0.036403574
531	2403	1069	6D	0.050401323
532	2407	1073	6D	0.018285046
533	2413	1074	6D	0.043704904
534	2416	1076	6D	0.041154475
535	2418	1078	6D	0.031477532
536	2424	1083	6D	0.003333529
537	2433	1087	6D	0.009536002
538	2435	1088	6D	0.039662467
539	2441	1089	6D	0.0129772
540	2442	1090	6D	0.030754742

continued on next page

–continued from previous page

Index	Partical #	Accumulated #(hitting the worm)	Nucleus	Edep(MeV)
541	2447	1093	6D	0.013849479
542	2449	1094	6D	0.027025338
543	2455	1096	6D	0.00732945
544	2463	1099	6D	0.016687435
545	2469	1104	6D	0.024205981
546	2471	1105	6D	0.036748161
547	2477	1106	6D	0.013225697
548	2487	1109	6D	0.04215514
549	2490	1111	6D	0.012855454
550	2491	1112	6D	0.034929435
551	2494	1114	6D	0.024621178
552	2498	1115	6D	0.019093452
553	2510	1119	6D	0.033622596
554	2516	1123	6D	0.0170597
555	2517	1124	6D	0.037415049
556	2521	1126	6D	0.000941014
557	2522	1127	6D	0.031419786
558	2530	1129	6D	0.044735785
559	2535	1130	6D	0.052680668
560	2537	1131	6D	0.038746634
561	2554	1138	6D	0.011742432
562	2555	1139	6D	0.035488524

continued on next page

–continued from previous page

Index	Partical #	Accumulated #(hitting the worm)	Nucleus	Edep(MeV)
563	2557	1140	6D	0.027697283
564	2558	1141	6D	0.037266759
565	2574	1149	6D	0.066674057
566	2576	1150	6D	0.052092932
567	2581	1153	6D	0.046584002
568	2582	1154	6D	0.043463934
569	2585	1155	6D	0.04011046
570	2589	1157	6D	0.034407537
571	2594	1158	6D	0.0176858
572	2596	1159	6D	0.039299235
573	2601	1160	6D	0.032431547
574	2607	1163	6D	0.048307133
575	2610	1166	6D	0.038489179
576	2616	1167	6D	0.026155491
577	2623	1171	6D	0.021950724
578	2625	1172	6D	0.01526354
579	2629	1175	6D	0.026436744
580	2630	1176	6D	0.02964393
581	2631	1177	6D	0.039482736
582	2632	1178	6D	0.038434777
583	2639	1180	6D	0.020893808
584	2651	1183	6D	0.002546853

continued on next page

–continued from previous page

Index	Partical #	Accumulated #(hitting the worm)	Nucleus	Edep(MeV)
585	2653	1185	6D	0.002474245
586	2655	1187	6D	0.036449692
587	2660	1188	6D	0.038737355
588	2666	1190	6D	0.059630898
589	2672	1192	6D	0.031554372
590	2675	1193	6D	0.11537018
591	2677	1194	6D	0.019695486
592	2679	1195	6D	0.026447707
593	2680	1196	6D	0.032517905
594	2682	1197	6D	0.048812743
595	2693	1199	6D	0.039126511
596	2702	1203	6D	0.037000608
597	2707	1204	6D	0.043431214
598	2709	1205	6D	0.031370493
599	2715	1207	6D	0.024750522
600	2726	1212	6D	0.047457577
601	2728	1214	6D	0.03434634
602	2732	1215	6D	0.030790586
603	2735	1217	6D	0.017570018
604	2736	1218	6D	0.037986531
605	2745	1221	6D	0.025643437
606	2755	1224	6D	0.000216613

continued on next page

–continued from previous page

Index	Partical #	Accumulated #(hitting the worm)	Nucleus	Edep(MeV)
607	2759	1225	6D	0.034951976
608	2761	1226	6D	0.024421594
609	2762	1227	6D	0.037849366
610	2769	1230	6D	0.034938967
611	2778	1232	6D	0.034932271
612	2780	1234	6D	0.008293457
613	2782	1235	6D	0.035675066
614	2786	1238	6D	0.006718394
615	2787	1239	6D	0.022482724
616	2789	1240	6D	0.041336402
617	2799	1244	6D	0.038990624
618	2811	1251	6D	0.000496086
619	2816	1254	6D	0.03981617
620	2817	1255	6D	0.026296569
621	2823	1257	6D	0.020874461
622	2832	1261	6D	0.062625363
623	2835	1263	6D	0.050873219
624	2849	1264	6D	0.01832529
625	2854	1267	6D	0.009818567
626	2856	1268	6D	0.046210344
627	2863	1271	6D	0.007179308
628	2864	1272	6D	0.046172022

continued on next page

–continued from previous page

Index	Partical #	Accumulated #(hitting the worm)	Nucleus	Edep(MeV)
629	2872	1276	6D	0.019879787
630	2878	1280	6D	0.007155505
631	2889	1283	6D	0.017961977
632	2901	1289	6D	0.035911673
633	2902	1290	6D	0.027566254
634	2905	1293	6D	0.00391899
635	2906	1294	6D	0.025982846
636	2920	1299	6D	0.013318211
637	2921	1300	6D	0.037526276
638	2923	1301	6D	0.042128108
639	2925	1302	6D	0.025335681
640	2930	1305	6D	0.04233088
641	2936	1307	6D	0.091117901
642	2942	1308	6D	0.024189723
643	2943	1309	6D	0.03441563
644	2947	1311	6D	0.00196772
645	2951	1312	6D	0.023241721
646	2952	1313	6D	0.049358815
647	2955	1314	6D	0.026609075
648	2986	1323	6D	0.04627446
649	2987	1324	6D	0.039336793
650	2989	1325	6D	0.040542557

continued on next page

–continued from previous page

Index	Partical #	Accumulated #(hitting the worm)	Nucleus	Edep(MeV)
651	2990	1326	6D	0.017100697
652	3001	1328	6D	0.046199577
653	3018	1335	6D	0.049481675
654	3021	1338	6D	0.038221339
655	3022	1339	6D	0.12464208
656	3029	1342	6D	0.042079455
657	3032	1344	6D	0.023110708
658	3035	1346	6D	0.030455443
659	3038	1349	6D	0.020013165
660	3041	1351	6D	0.014635895
661	3045	1352	6D	0.044142903
662	3061	1358	6D	0.015943711
663	3063	1359	6D	0.040776761
664	3064	1360	6D	0.020940551
665	3068	1362	6D	0.045856966
666	3069	1363	6D	0.026526452
667	3077	1365	6D	0.017597257
668	3092	1372	6D	0.026916417
669	3094	1374	6D	0.040323331
670	3095	1375	6D	0.03331024
671	3096	1376	6D	0.030228355
672	3100	1379	6D	0.015819832

continued on next page

–continued from previous page

Index	Partical #	Accumulated #(hitting the worm)	Nucleus	Edep(MeV)
673	3101	1380	6D	0.046222895
674	3105	1382	6D	0.05436895
675	3114	1385	6D	0.037953599
676	3118	1386	6D	0.051604225
677	3124	1390	6D	0.041068131
678	3126	1391	6D	0.019567209
679	3129	1392	6D	0.041173294
680	3130	1393	6D	0.041235008
681	3131	1394	6D	0.034568063
682	3141	1398	6D	0.041564312
683	3150	1402	6D	0.034994058
684	3156	1405	6D	0.034823618
685	3161	1407	6D	0.00605431
686	3163	1408	6D	0.041107397
687	3167	1409	6D	0.033409572
688	3168	1410	6D	0.016669822
689	3169	1411	6D	0.025711777
690	3173	1414	6D	0.03657123
691	3176	1416	6D	0.048249501
692	3180	1418	6D	0.03186898
693	3183	1420	6D	0.043724297
694	3184	1421	6D	0.044338117

continued on next page

–continued from previous page

Index	Partical #	Accumulated #(hitting the worm)	Nucleus	Edep(MeV)
695	3188	1423	6D	0.022160784
696	3190	1425	6D	0.039273824
697	3192	1427	6D	0.030451941
698	3199	1428	6D	0.009610252
699	3201	1429	6D	0.031477222
700	3202	1430	6D	0.050732515
701	3204	1431	6D	0.026375333
702	3207	1433	6D	0.017397289
703	3224	1440	6D	0.024031111
704	3225	1441	6D	0.027286323
705	3226	1442	6D	0.001921861
706	3232	1444	6D	0.039563794
707	3243	1450	6D	0.009538079
708	3249	1452	6D	0.063038519
709	3257	1456	6D	0.016130393
710	3262	1457	6D	0.041941356
711	3268	1459	6D	0.016940033
712	3270	1460	6D	0.053559157
713	3284	1465	6D	0.033773149
714	3289	1467	6D	0.045977818
715	3292	1469	6D	0.002954058
716	3297	1472	6D	0.173318261

continued on next page

–continued from previous page

Index	Partical #	Accumulated #(hitting the worm)	Nucleus	Edep(MeV)
717	3299	1473	6D	0.004598896
718	3301	1474	6D	0.040226936
719	3304	1476	6D	0.01571909
720	3307	1477	6D	0.041700758
721	3310	1478	6D	0.040639346
722	3312	1479	6D	0.067994812
723	3320	1481	6D	0.044376888
724	3334	1486	6D	0.035811495
725	3339	1487	6D	0.047032112
726	3341	1489	6D	0.04559723
727	3346	1492	6D	0.019450861
728	3349	1493	6D	0.025628362
729	3352	1496	6D	0.039226712
730	3354	1497	6D	0.040643397
731	3363	1501	6D	0.041073106
732	3367	1503	6D	0.040976693
733	3368	1504	6D	0.028814595
734	3372	1506	6D	0.018193487
735	3373	1507	6D	0.040000275
736	3375	1509	6D	0.045837227
737	3376	1510	6D	0.032307266
738	3377	1511	6D	0.00144572

continued on next page

–continued from previous page

Index	Partical #	Accumulated #(hitting the worm)	Nucleus	Edep(MeV)
739	3386	1515	6D	0.042786603
740	3389	1517	6D	0.04486173
741	3390	1518	6D	0.026306985
742	3392	1519	6D	0.014136683
743	3393	1520	6D	0.036780646
744	3394	1521	6D	0.041464512
745	3399	1524	6D	0.020718965
746	3406	1525	6D	0.019755348
747	3415	1529	6D	0.040292141
748	3417	1531	6D	0.043605544
749	3418	1532	6D	0.05337411
750	3421	1533	6D	0.020736185
751	3422	1534	6D	0.036510761
752	3425	1535	6D	0.021654305
753	3431	1536	6D	0.00217258
754	3434	1537	6D	0.023023316
755	3436	1539	6D	0.027981114
756	3437	1540	6D	0.028699631
757	3444	1543	6D	0.02823922
758	3447	1545	6D	0.032162797
759	3453	1547	6D	0.043710713
760	3455	1548	6D	0.022027967

continued on next page

–continued from previous page

Index	Partical #	Accumulated #(hitting the worm)	Nucleus	Edep(MeV)
761	3462	1551	6D	0.049473655
762	3463	1552	6D	0.044124443
763	3464	1553	6D	0.003631459
764	3470	1555	6D	0.039013648
765	3473	1556	6D	0.046177575
766	3474	1557	6D	0.030113662
767	3476	1558	6D	0.010406717
768	3480	1560	6D	0.030351757
769	3485	1565	6D	0.011375205
770	3489	1567	6D	0.049282712
771	3490	1568	6D	0.036521508
772	3492	1569	6D	0.007351374
773	3496	1570	6D	0.091337952
774	3501	1573	6D	0.030743466
775	3507	1574	6D	0.02246645
776	3510	1576	6D	0.04406188
777	3515	1577	6D	0.001170225
778	3517	1578	6D	0.04404092
779	3521	1579	6D	0.059496437
780	3523	1580	6D	0.03564808
781	3528	1583	6D	0.006225844
782	3530	1585	6D	0.004950678

continued on next page

–continued from previous page

Index	Partical #	Accumulated #(hitting the worm)	Nucleus	Edep(MeV)
783	3533	1587	6D	0.046381526
784	3537	1588	6D	0.033004537
785	3540	1589	6D	0.0008693
786	3555	1594	6D	0.032589975
787	3559	1595	6D	0.007489924
788	3561	1596	6D	0.013469308
789	3564	1599	6D	0.022029734
790	3565	1600	6D	0.098980304
791	3570	1603	6D	0.033634459
792	3573	1606	6D	0.04052971
793	3579	1607	6D	0.025832542
794	3592	1610	6D	0.044362692
795	3606	1611	6D	0.013513856
796	3614	1617	6D	0.033262769
797	3615	1618	6D	0.035330586
798	3616	1619	6D	0.02969494
799	3618	1620	6D	0.077499802
800	3624	1622	6D	0.062411033
801	3632	1624	6D	0.030547033
802	3633	1625	6D	0.034679952
803	3644	1627	6D	0.001964207
804	3647	1629	6D	0.037346223

continued on next page

–continued from previous page

Index	Partical #	Accumulated #(hitting the worm)	Nucleus	Edep(MeV)
805	3651	1631	6D	0.047839243
806	3652	1632	6D	0.023706708
807	3653	1633	6D	0.047743683
808	3655	1634	6D	0.034192145
809	3661	1636	6D	0.006083235
810	3668	1639	6D	0.012117849
811	3682	1648	6D	0.011092662
812	3685	1649	6D	0.04579138
813	3687	1651	6D	0.049989153
814	3688	1652	6D	0.237097443
815	3694	1654	6D	0.038437309
816	3705	1657	6D	0.036184235
817	3707	1659	6D	0.044470886
818	3713	1661	6D	0.008733547
819	3714	1662	6D	0.001635001
820	3718	1663	6D	0.004387666
821	3719	1664	6D	0.055583555
822	3724	1665	6D	0.043584704
823	3727	1666	6D	0.018006652
824	3731	1667	6D	0.012984535
825	3736	1668	6D	0.022092933
826	3740	1670	6D	0.020960141

continued on next page

–continued from previous page

Index	Partical #	Accumulated #(hitting the worm)	Nucleus	Edep(MeV)
827	3750	1675	6D	0.188574586
828	3751	1676	6D	0.016964323
829	3759	1677	6D	0.021254714
830	3763	1679	6D	0.04005182
831	3771	1681	6D	0.034277798
832	3774	1684	6D	0.045489921
833	3775	1685	6D	0.043928109
834	3790	1690	6D	0.045908288
835	3791	1691	6D	0.034875759
836	3794	1692	6D	0.026426476
837	3797	1694	6D	0.042171515
838	3807	1695	6D	0.021473015
839	3814	1697	6D	0.017297993
840	3818	1698	6D	0.034144966
841	3819	1699	6D	0.043807625
842	3824	1702	6D	0.025084285
843	3825	1703	6D	0.024092782
844	3827	1705	6D	0.056649832
845	3829	1706	6D	0.085248334
846	3830	1707	6D	0.03620892
847	3831	1708	6D	0.041309255
848	3836	1710	6D	0.051837483

continued on next page

–continued from previous page

Index	Partical #	Accumulated #(hitting the worm)	Nucleus	Edep(MeV)
849	3845	1714	6D	0.025897221
850	3848	1717	6D	0.031272789
851	3851	1719	6D	0.038248911
852	3853	1720	6D	0.03288015
853	3857	1723	6D	0.016977286
854	3860	1724	6D	0.033827322
855	3862	1726	6D	0.031542403
856	3870	1729	6D	0.043341847
857	3871	1730	6D	0.036302962
858	3875	1732	6D	0.037071933
859	3876	1733	6D	0.016360191
860	3877	1734	6D	0.050705975
861	3882	1735	6D	0.020008329
862	3887	1738	6D	0.032584174
863	3891	1740	6D	0.036729857
864	3893	1741	6D	0.029459958
865	3896	1742	6D	0.04169591
866	3904	1743	6D	0.018956934
867	3909	1746	6D	0.037195348
868	3915	1748	6D	0.04142808
869	3918	1749	6D	0.034733388
870	3926	1751	6D	0.054713918

continued on next page

–continued from previous page

Index	Partical #	Accumulated #(hitting the worm)	Nucleus	Edep(MeV)
871	3928	1752	6D	0.035646083
872	3929	1753	6D	0.024546556
873	3936	1755	6D	0.065042078
874	3945	1761	6D	0.048483958
875	3952	1764	6D	0.004238233
876	3954	1765	6D	0.013845195
877	3957	1766	6D	0.042499725
878	3961	1767	6D	0.037582977
879	3965	1768	6D	0.039308081
880	3970	1770	6D	0.057112207
881	3972	1772	6D	0.009822478
882	3975	1775	6D	0.04331519
883	3983	1777	6D	0.044812809
884	4002	1784	6D	0.024805028
885	4010	1786	6D	0.018813112
886	4016	1789	6D	0.017875373
887	4025	1791	6D	0.045886844
888	4028	1792	6D	0.010140598
889	4031	1793	6D	0.007448216
890	4040	1795	6D	0.03606586
891	4044	1798	6D	0.026463933
892	4047	1800	6D	0.034972285

continued on next page

–continued from previous page

Index	Partical #	Accumulated #(hitting the worm)	Nucleus	Edep(MeV)
893	4054	1802	6D	0.03397536
894	4056	1804	6D	0.02330034
895	4062	1807	6D	0.017453518
896	4064	1808	6D	0.071111112
897	4065	1809	6D	0.033238495
898	4069	1811	6D	0.030775729
899	4071	1812	6D	0.019207714
900	4075	1813	6D	0.028693092
901	4083	1817	6D	0.01811038
902	4084	1818	6D	0.020805844
903	4087	1819	6D	0.046002561
904	4098	1822	6D	0.021409787
905	4111	1824	6D	0.029425935
906	4126	1827	6D	0.039764236
907	4141	1833	6D	0.030870877
908	4144	1834	6D	0.033714537
909	4157	1837	6D	0.040106693
910	4166	1839	6D	0.041112717
911	4168	1841	6D	0.01161997
912	4169	1842	6D	0.014518857
913	4175	1845	6D	0.032793169
914	4182	1847	6D	0.005618414

continued on next page

–continued from previous page

Index	Partical #	Accumulated #(hitting the worm)	Nucleus	Edep(MeV)
915	4183	1848	6D	0.030994774
916	4185	1849	6D	0.021747868
917	4186	1850	6D	0.042612175
918	4193	1852	6D	0.015887387
919	4222	1864	6D	0.04493718
920	4223	1865	6D	0.017580625
921	4224	1866	6D	0.039506599
922	4232	1869	6D	0.038316518
923	4234	1870	6D	0.048455008
924	4238	1872	6D	0.034803644
925	4239	1873	6D	0.011174847
926	4240	1874	6D	0.023409755
927	4244	1877	6D	0.026135286
928	4263	1885	6D	0.046911239
929	4276	1891	6D	0.031891715
930	4279	1893	6D	0.032534287
931	4298	1899	6D	0.033468877
932	4304	1900	6D	0.030856422
933	4311	1902	6D	0.042299223
934	4315	1904	6D	0.035575214
935	4317	1906	6D	0.013987039
936	4321	1908	6D	0.051982881

continued on next page

–continued from previous page

Index	Partical #	Accumulated #(hitting the worm)	Nucleus	Edep(MeV)
937	4323	1910	6D	0.026483795
938	4325	1912	6D	0.014362767
939	4330	1913	6D	0.059549649
940	4336	1916	6D	0.012437025
941	4337	1917	6D	0.042254219
942	4346	1920	6D	0.033115554
943	4351	1923	6D	0.034010256
944	4353	1925	6D	0.035810128
945	4355	1926	6D	0.034440035
946	4356	1927	6D	0.035806039
947	4359	1928	6D	0.057908403
948	4362	1930	6D	0.028191661
949	4366	1931	6D	0.050985574
950	4367	1932	6D	0.032430109
951	4370	1933	6D	0.032880542
952	4372	1934	6D	0.036944771
953	4378	1936	6D	0.039298284
954	4385	1940	6D	0.014636537
955	4386	1941	6D	0.02099024
956	4398	1948	6D	0.021798191
957	4415	1955	6D	0.047880491
958	4419	1956	6D	0.040205229

continued on next page

–continued from previous page

Index	Partical #	Accumulated #(hitting the worm)	Nucleus	Edep(MeV)
959	4429	1961	6D	0.022578951
960	4431	1963	6D	0.025575823
961	4436	1965	6D	0.033468144
962	4438	1966	6D	0.017365337
963	4445	1969	6D	0.022947087
964	4446	1970	6D	0.016605864
965	4449	1972	6D	0.041394043
966	4452	1973	6D	0.045287527
967	4453	1974	6D	0.033654498
968	4454	1975	6D	0.048146395
969	4464	1977	6D	0.011215573
970	4468	1979	6D	0.029236177
971	4478	1983	6D	0.040586154
972	4496	1992	6D	0.069032911
973	4498	1993	6D	0.020812452
974	4501	1994	6D	0.052900818
975	4507	1997	6D	0.019757223
976	4510	1998	6D	0.040017422
977	4512	1999	6D	0.021991293
978	4518	2002	6D	0.004665665
979	4520	2004	6D	0.022926411
980	4524	2006	6D	0.034075846

continued on next page

–continued from previous page

Index	Partical #	Accumulated #(hitting the worm)	Nucleus	Edep(MeV)
981	4534	2011	6D	0.031420434
982	4541	2017	6D	0.027935551
983	4548	2021	6D	0.006427705
984	4557	2027	6D	0.044165442
985	4558	2028	6D	0.032540462
986	4563	2031	6D	0.029846889
987	4571	2033	6D	0.004254036
988	4575	2035	6D	0.033736791
989	4583	2037	6D	0.032396436
990	4584	2038	6D	0.04230115
991	4608	2049	6D	0.02660844
992	4610	2050	6D	0.001265371
993	4611	2051	6D	0.041442329
994	4621	2056	6D	0.045456899
995	4623	2057	6D	0.046858524
996	4628	2059	6D	0.036253146
997	4633	2061	6D	0.037899169
998	4640	2063	6D	0.029914143
999	4641	2064	6D	0.028484511
1000	4643	2065	6D	0.008017189